Artificial deep neural network modeling of solar- and atmospheric-driven ground magnetic perturbations at mid-latitude

Rungployphan Kieokaew[1], Veronika Haberle[1,2], Aurélie Marchaudon[1], Pierre-Louis Blelly[1], Aude Chambodut[3,4]

[1]Institut de Recherche en Astrophysique et Planétologie, Université de Toulouse, CNRS, CNES, Toulouse, France
[2]Conrad Observatory, GeoSphere Austria, Vienna, Austria
[3]Université de Strasbourg, CNRS, ITES UMR 7063, F-67000 Strasbourg, France
[4]Université de Strasbourg, CNRS, EOST UAR 830, F-67000 Strasbourg, France

Key Points:

- We model solar- and atmospheric-driven magnetic perturbations at Chambon-la-Forêt observatory using long short-term memory neural networks.
- Two neural networks are built to model the above-diurnal and the daily variations using the walk forward training.
- This work demonstrates capability of our approach with important application for near real-time calculation of magnetic activity indices.

Corresponding author: Rungployphan Kieokaew, rkieokaew@irap.omp.eu

Abstract

Ground magnetic observatories measure the Earth's magnetic field and its coupling with the solar wind responsible for ionospheric and magnetospheric current systems. Predicting effects of solar- and atmospheric-driven disturbances is a crucial task. Using data from the magnetic observatory Chambon-la-Forêt at mid-latitude, we investigate the capability of our developed deep artificial neural networks in the modeling of the contributions above 24 hours and the daily variations. Two neural networks were built with the long short-term memory architecture with multiple layers. Using the data from 1995 onwards, the neural networks were trained with physical parameters indicative of solar variabilities and geographical daily and seasonal variations. By excluding the secular variation owing to the change of the Earth's intrinsic magnetic field, we demonstrate that our approach can model the observed signals with overall good agreements for both a solar-quiet period in 2009 and a solar-active period in 2012. Particularly, using the walk forward training, we updated our models with new data leading up to the test year. The implication of this work is twofold. First, our approach can be adapted for near real-time prediction of intensity of solar and atmospheric disturbances. Second, the neural networks can be used to model the quiet variations when excluding the solar variabilities with important applications in the calculation of magnetic activity indices. This work is a proof-of-concept that deep neural networks can be used to model solar- and atmospheric-driven perturbations modulated by daily and seasonal variations as recorded at a ground magnetic observatory.

Plain Language Summary

The Sun and its activities interact with the Earth's magnetic field with effects measurable on the ground. Magnetic activity indices derived from ground magnetic observatories measure the intensity of the Sun-magnetosphere-ionosphere and neutral atmosphere coupling; they are crucial parameters in which the space weather-related operations rely on. The Kp index derived from several observatories at mid-latitude has been the most widely used. Yet, its time cadence (3h) and intensity scale (0 to 9) are rather crude. Besides, it is challenging to determine a geomagnetic 'baseline' indicative of 'quiet' variations in the absence of solar-driven perturbations in which the Kp index was derived. In an effort to derive a new index with higher cadence and finer intensity scale, we consider an application of machine-learning neural networks to model the ground magnetic perturbations owing to the Sun-Earth coupling for both quiet periods, i.e., in the absence of solar storms, and active period, using first data from the observatory Chambon-la-Forêt, France. Particularly, we consider modeling a baseline using the solar irradiance and parameters indicative of daily and seasonal variations. Our work shows promising results demonstrating its potential applicability for near real-time calculation of a new magnetic index.

1 Introduction

Magnetic observatories at the ground level measure a superposition of magnetic fields of several sources at certain geographical locations. The dominant source is the Earth's intrinsic magnetic field, also called the "main field", generated by geodynamo processes in the Earth's fluid inner core. The main field contributes over 93 % of the magnitude of the magnetic measurements at the surface, about tens of thousands of nano teslas (nT). Another internal source is the magnetized lithosphere which contributes to smaller scale variations (e.g., Thébault et al., 2010). Other sources contributing to the geomagnetic field are electric currents flowing in the ionosphere and magnetosphere. In the ionosphere, the solar quiet (Sq) current in low- and mid-latitudes in the E-region is a dominant source that gives rise to the regular daily variations on the order of tens of nT (e.g., Yamazaki & Maute, 2017). It forms on the sunlit side as powered by the so-

lar irradiance. The Sq variations are believed to be affected by tidal waves of atmospheric origins, which are global-scale oscillations with harmonic periods of a day. Along the magnetic equator, a strong zonal current forms a belt known as the equatorial electrojet (EEJ; Chapman, 1951). At high latitudes, there are auroral electrojets (AEJ) driven by the ionospheric-solar dynamo. Depending on the energy input by the solar wind through convection and particle precipitation, the auroral ionospheric conductivities vary and give rise to AEJ, marking the auroral ovals in the northern and southern hemispheres. In the magnetosphere, current systems such as the ring current and field-aligned currents are significantly enhanced during solar events and modulate the geomagnetic field.

The solar wind and the interplanetary magnetic field (IMF) interact with the Earth's magnetic field through complex couplings in several regions from the bow shock down to the ionosphere and the ground level. Ground magnetic measurements are thus valuable data sources for studying effects of the solar-driven disturbances on the magnetospheric and ionospheric systems. Solar-driven disturbances including solar storms affect the overall magnetospheric-ionospheric systems that enhance current systems and govern complex interaction among them. Solar storms are solar transient structures that can disturb the Earth's magnetic field temporarily and consequently trigger geomagnetic storms involving magnetic reconnection at the Earth's magnetopause and in the magnetotail. Interplanetary coronal mass ejection (ICME) is a major type of solar disturbances caused by an eruption on the solar surface. Earth-directed ICMEs have effects measurable on the ground from a few days up to a week. Corotating interaction region (CIR) is another transient structure formed when the fast solar wind originated from the Sun's coronal holes takes over a slower wind. The compression region and high-speed wind embedded in CIRs can also disturbed the geomagnetic field up to several days. Characterization of the intensity or effects of these solar storms on the various systems is a vital task of the space weather community.

Magnetic activity indices characterizing the intensity of solar-terrestrial activities are derived from ground magnetic measurements. K-indices were first introduced by Bartels et al. (1939) to indicate the level of the perturbations with respect to a regular variation at a 3-hour range at mid-latitude. The K-indices were derived for the Niemegk observatory with a scale of 0 (quiet) to 9 (strongly disturbed); this scale is then mapped to other observatories. These K-indices were later standardized as Ks-indices for 13 mid-latitude observatories. The Kp (K-planetary) index was then defined as the average of the Ks-indices (Bartels, 1949). Since their first conception, more geomagnetic indices have been proposed and concretized. Other K-derived indices include aa that was derived from two antipodal observatories from which the longest time series are available. The am, an, and as indices were proposed by Mayaud (1968) to indicate sub-auroral magnetic activities at global, northern and southern scales. A comprehensive review of magnetic activity indices can be found in Menvielle et al. (2011). To derive these indices, we need to establish a geomagnetic "baseline" that characterizes quiet magnetic variations in the absence of solar disturbances. The quiet variations refer specifically to the measurements with no significant external influences or sudden changes as mentioned next.

The quiet magnetic variations traditionally involved hand-scaling from analogue magnetograms by well-trained observers. Bartels et al. (1939) defined the regular daily variation as "a smooth curve to be expected for that element on a magnetically quiet day, according to the season, the sunspot cycle and, in some cases, the phase of the Moon". With the rise of the digital age, algorithms to automatically generate K indices were proposed (see Menvielle et al., 1995). These algorithms involved an estimation of the non-K variations that are the quiet variations according to the so-called Bartels-Mayaud rules (Mayaud, 1967). The Finnish Meteorological Institute (FMI) method (Sucksdorff et al., 1991) was found to be the most suitable for the continuation of K-indices series without any serious jump in the statistics when passing from analog to numerical determination at one magnetic observatory (Menvielle et al., 1995). Four algorithms including

the FMI method have been endorsed by the IAGA (International Association of Geomagnetism and Aeronomy; `https://www.iaga-aiga.org/`). Another proposed method adopted for the SuperMAG data processing to determine the baseline involves a decomposition of sources of the measured field (Gjerloev, 2012). Due to the lack of ground truth and clear identification of quiet sources, the subtraction of these empirically-derived baselines from ground magnetic measurements may not reflect the real intensity of solar-driven perturbations. Thus, the magnitude of such perturbations may be underestimated or overestimated. This can have serious impacts on space weather applications and warnings.

To distinguish the perturbations of solar origin in the signals from other sources, establishing the geomagnetic baseline that robustly represents quiet periods is thus imperative. In an effort to derive a new magnetic activity index with a higher time resolution, Haberle et al. (2022) proposed to characterize the magnetic measurements during quiet periods by filtering the signals into the above-diurnal (>24 hr), diurnal (24 hr), and sub-diurnal variations to capture physical sources at specific time scales and combine them to determine the geomagnetic baseline. This approach works rather well during quiet periods. It is efficient; it does not need any a priori information, thus it is scalable and suitable for near-real time applications. However, in the presence of solar-driven disturbances, the perturbations are present in all of the filters that were supposed to represent the quiet variations. Consequently, the actual intensity of solar-driven perturbations can be underestimated. Moreover, they compared their results to the FMI and SuperMAG methods. It turns out that the baseline from the FMI method follows the geomagnetic-storm variation similar to the filtering approach while the baseline from SuperMAG is less sensitive to the storm variation. There is thus still a need to robustly establish the baseline that contains quiet variations with minimal influence of storm perturbations.

In this work, we consider an application of machine learning for modeling solar- and atmospheric-driven ground magnetic perturbations. Deriving a geomagnetic baseline and a magnetic activity index requires careful, dedicated studies. As a first step, we consider also the machine-learning based modeling of a geomagnetic baseline representative of the regular, quiet variations. Our goal is to be able to produce a baseline that is not influenced by geomagnetic storms while robustly accounting for the main internal sources and the Sq variation and its possible day-to-day variability. We limit our focus to mid-latitude. Since Haberle et al. (2022) have already decomposed the ground magnetic measurements to several contributions, we take these data as a starting point with the aim to demonstrate the capability of machine-learning based approach. Specifically, we consider using neural networks for regression (i.e. time-series) modeling as they allow us to consider independent parameters associated with physical sources contributing to the magnetic measurements. Neural networks have increasingly been used for space-weather related applications including prediction of magnetic activity indices (e.g., Wu & Lundstedt, 1996; Kumluca et al., 1999; Stepanova & Pérez, 2000; Wintoft & Cander, 2000; Lundstedt et al., 2002; Uwamahoro & Habarulema, 2014; Shin et al., 2016; Zhelavskaya et al., 2017; Tebabal et al., 2018; Efitorov et al., 2018; Gruet et al., 2018; Jackson et al., 2020; Zou et al., 2020; Chakraborty & Morley, 2020; Myagkova et al., 2021; Abuelezz et al., 2021; Siciliano et al., 2021; Collado-Villaverde et al., 2021; Madsen et al., 2022; Zhang et al., 2022; Huang et al., 2022; Bernoux et al., 2022; Collado-Villaverde et al., 2023; Vladimirov et al., 2023). We will demonstrate the capability of our newly developed neural networks during quiet periods as well as disturbed periods and discuss future applications.

The organization of our paper is as follows. We first describe data in Section 2. We next introduce the neural networks and workflow in Section 3. Then, we report the modeling results and performance in Section 4. Finally, we present a discussion in Section 5 and provide a summary and perspectives in Section 6.

2 Data

2.1 Ground magnetic data

We focus on data from the magnetic observatory Chambon-la-Forêt (CLF) located at mid-latitude (48.0250N, 2.2600E) in France, Europe. The data are available at Bureau Central de Magnétisme Terrestre data repository from 1936 onwards. The data are replicated and associated with worldwide magnetic observatory data at the International Real-time Magnetic Observatory Network (INTERMAGNET) for the period from 1991 onwards. From Haberle et al. (2022), the data were processed from 1991 to 2019. The measurements were made at 1-min cadence. The data are provided in a local cartesian coordinate system (NED: North, East, Down). The X-axis corresponds to the geographic north, the Y-axis corresponds to the geographic east, and the Z-axis completes the orthogonal system such that it directs towards the Earth's core. An example of the magnetic measurements at CLF can be found in the Supplementary Information (SI).

In an effort to distinguish contributions from several sources to the ground magnetic measurements, Haberle et al. (2022) first applied signal processing techniques to filter the measurement data. Using Finite Impulse Response filters, they decomposed the measurement data into the contributions at various time-scales as the following. Firstly, the above-diurnal contribution correspond to the variation in the signals above 24 ($f_{>24}$) hours. Secondly, the diurnal and semi-diurnal contributions correspond to the variation at 24 (f_{24}) and 12 (f_{12}) hours, respectively. Finally, the contributions at 8 (f_8) and 6 (f_6) hours were also derived. To keep the same notation as Haberle et al. (2022), we call these various contributions as "filter data". Using measurement data from observatories at low to mid latitudes in both northern and southern hemispheres, Haberle et al. (2022) demonstrated that the derived filter data capture the physical sources contributing to the measurements reasonably well. For instance, the $f_{>24}$ trends are dominated by the secularly varying magnetic strength associated with the local change of the Earth's intrinsic magnetic field. The diurnal and semi-diurnal trends, in contrast, are modulated by the season, the local time, and the day-to-day variation (see Campbell, 1989, and references therein). Haberle et al. (2022) combine all these filter data to determine a geomagnetic baseline during quiet periods.

Our work considers using the filter data individually as well as a combination of them. Since using the full resolution (1-min) data in the neural networks is computationally expensive, as a first step, we consider using the filter data at a lower time cadence. Taking the original 1-min filter data, we perform a decimation to obtain the data at every hour, i.e., at every HH:00 where HH is a given hour from 01, 02, 03, ... to 23. When considering an individual filter, e.g., the f_{24}, we decimate them directly. When considering a combination of the filters, e.g., the sum of the f_{24}, f_{12}, f_8, and f_6, we first sum them at the original 1-min cadence before decimating them. As a test, we also produced lower resolution data via a decimation to obtain data at every 15 minutes for the f_8, and f_6; their results are nearly identical to the results using 1-hour cadence data. The results in this work are thus produced using the 1-hour cadence filter data.

2.2 Solar wind and solar radio flux data

Solar wind conditions and solar variabilities drive the perturbation in the geomagnetic field. To get parameters relevant to these conditions, we utilize data products from the in-situ observations made upstream of the Earth at the Lagrangian L1 point as follows. We obtain the solar wind magnetic field and plasma datasets that are time-shifted to the Earth's bow shock nose (King & Papitashvili, 2005) from CDAWeb (Coordinated Data Analysis Web). Specifically, we use the OMNI combined, definitive 5-min resolution IMF and plasma data. For this data product, the data are available from 1995 onwards. We note that we have also tried the 1-hour merged OMNI data product, but the modeling results are somewhat poorer. The IMF data were obtained in the geocentric

solar magnetic (GSM) coordinates, labelled as B_x, B_y, and B_z, where X-axis points towards the Sun, Z-axis corresponds to the geomagnetic north, and Y-axis completes the right-hand orthonormal system. The plasma parameters were obtained for the proton bulk flow speed (V), the proton number density (N), and the proton temperature ($Temp$). These solar wind data are downsampled to 1 hour cadence using linear interpolation to reduce noise or local effects upstream of the bow shock. Besides, we performed a running average using the window size of 24 hours, centered on the considered data point, to further smooth the data. Without this smoothing, the modeling results would appear qualitatively noisy compared to the filter data. In addition, we obtain the daily 10.7 cm solar radio flux (F10.7) from the OMNI combined, definitive, and hourly product. The F10.7 is an important indicator of the solar activity, derived from a measurement of the flux density computed from the total emission at 10.7 cm wavelength from all sources present on the solar disk made over 1 hour period (Tapping, 2013). An example of these parameters can be found in the SI.

2.3 Geometrical data

Measurements at a magnetic observatory are influenced by the geographical location of the station (i.e. northern/southern hemisphere), the local time (i.e. day/night), and the season (i.e. the position of Earth around the Sun). Thus, parameters that record these variabilities, so-called "geometrical parameters" are relevant. We chose the solar zenith angle (SZA) and the solar longitude (Ls), in addition to the local time (LT) derived from the time stamps of the data. The SZA is the angle measured from directly above the observation point (zenith) to the elevation of the Sun in the sky, measured from the horizon. The Ls is the ecliptic longitude of the Sun; it indicates the position of the Earth around the Sun which relates to the seasons. The Ls is defined as 0^o at spring equinox in the northern hemisphere, 90^o at summer solstice, 180^o at autumn equinox, and 270^o at winter solstice. All these parameters are indicative of daily and seasonal variations (see examples of these parameters in the SI).

3 Neural network and workflow

3.1 Neural network description and workflow

We develop a neural network with multiple input features and multiple output targets. The multiple input features are to accommodate the independent variables including the solar wind IMF and plasma, the solar radio flux, and the geometrical parameters. The multiple output targets are set to accommodate the dependent variables consisting in the three components (X, Y, Z) of the filter data. Fig 1 shows a schematic diagram of the artificial neural network architecture for the above-diurnal filter. The neural network is built using the TensorFlow Keras module (Abadi et al., 2015).

We set up two main neural networks. The first one is to model the above-diurnal filter ($f_{>24}$) for all of the three components ($x_{>24}$, $y_{>24}$, $z_{>24}$), as shown in Fig 1. The $f_{>24}$ filter contains effects driven by the solar wind IMF and plasma variations, despite being dominated by the secular variations owing to the internal geomagnetic change as will be discussed in detail in Section 4.1. Next, a second neural network is set up to model the sum of other contributions: the diurnal (f_{24}), semi-diurnal (f_{12}), and 8 hr (f_8) and 6 hr (f_6). We call the sum of the other contributions as the daily filter or f_D. This second neural network has the same inputs and the same neural network architecture, but with different output targets being x_D, y_D, and z_D. The f_D is mainly dominated by the periodic variation with a period of one day as modulated by the geometrical parameters. Additionally, we also tested setting up individual neural networks for the diurnal and sub-diurnal filters; the sum of the modeling results are equivalent to modeling the f_D directly (while taking more computational resources).

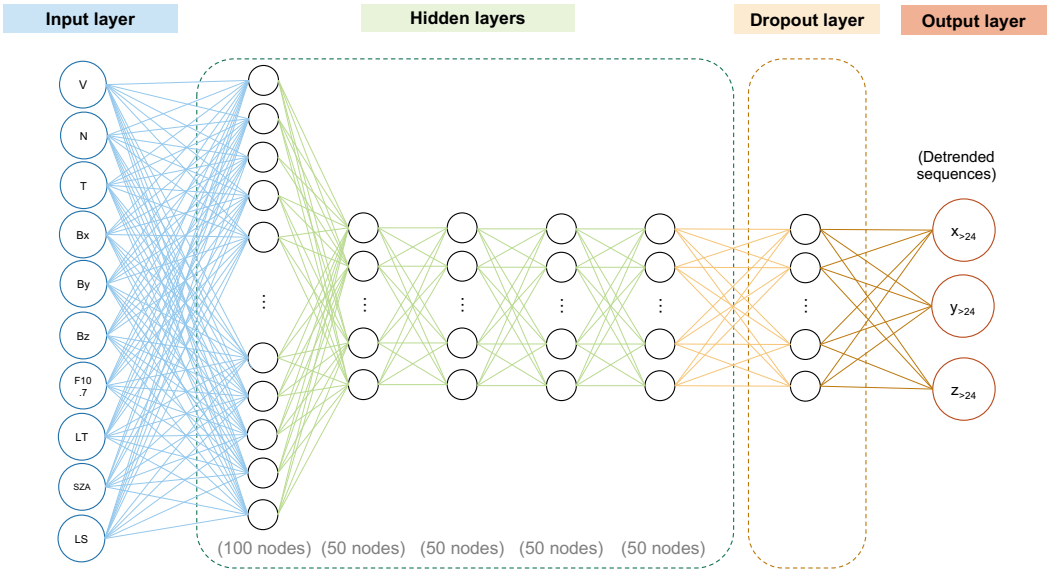

Figure 1. Diagram of the neural network architecture. The input layer (left) takes solar wind IMF and plasma parameters, the solar radio flux, and the geometrical parameters. The output layer (right) yields the three components (X, Y, Z) of the filter data, shown for the above-diurnal filter in this diagram. The hidden layers comprise 5 layers, with certain numbers of nodes for the individual layers. A dropout layer is added between the last hidden layer and the output layer to avoid overfitting. Each layer is an LSTM recurrent neural network layer (see text).

Since we set up two neural networks, we prepare two separate workflows for the above-diurnal filter and the daily filter. Fig 2 shows workflow diagrams for modeling $f_{>24}$ (Fig 2a) and f_D (Fig 2b). The final modeling outputs are the sum of the modeled f¿24 and fD as indicated in Fig 2c. The $f_{>24}$ and f_D require different pre-processing and post-processing steps; these will be described in Section 4. Apart from those steps, the two workflows have identical processes (a2 and b2 in Fig 2) for scaling and then structuring the data before the modeling with the neural network. The scaling part is a usual routine for machine learning in order to standardize or normalize the data, which helps improve the performance of machine learning algorithms.

Since the ground magnetic measurements comprise the responses from the solar-wind and atmospheric conditions influencing the magnetospheric and ionospheric currents, the neural network must be able to account for the history of such conditions and/or physical processes. For this reason, we chose the Long Short-Term Memory (LSTM) that is a recurrent neural network (Hochreiter & Schmidhuber, 1997). In principal, this type of neural network can keep track of the dependencies in the input sequences. Through the learning process, the neural network can memorize past input sequences that will likely affect the present and future data. We set our default time window of the history to be 30 hours. This 30-hr window was chosen based on a cross-correlation analysis between the solar wind speed and the variation in the $x_{>24}$ filter, which is in general most sensitive to perturbations induced by the solar wind. Using each month of data of two representative years for a solar minimum (2009) and a solar maximum (2012), the best correlation coefficients (above 0.5) were found for the time lags between 0.6 and 12 hours, depending on the average solar wind speed. This 30-hour window is sufficiently long to take into account the time response of the magnetospheric-ionospheric systems in the order of several hours.

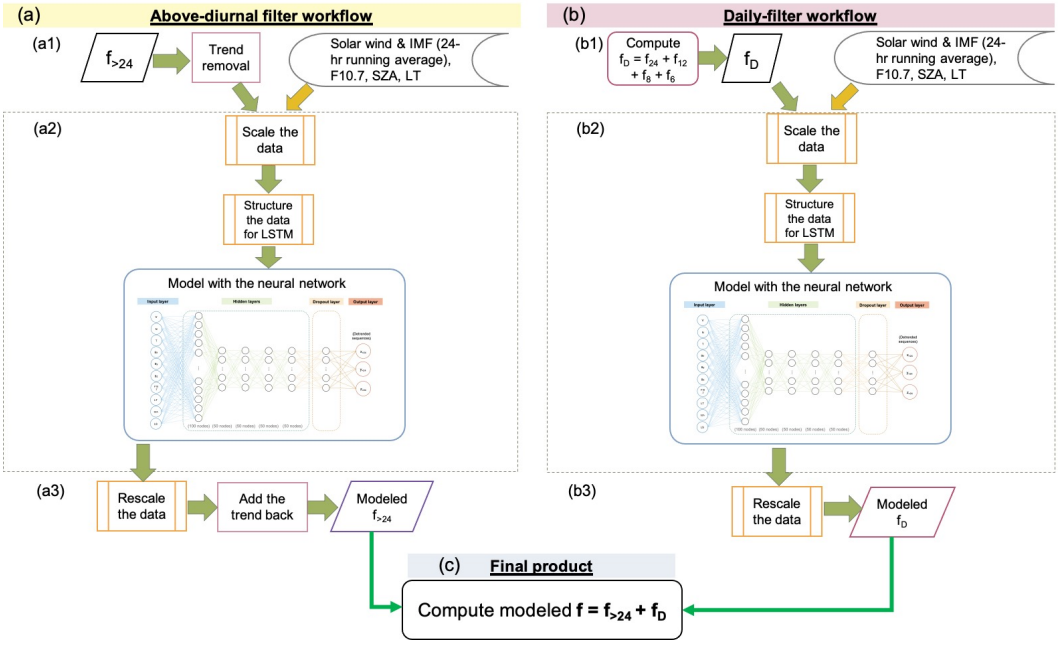

Figure 2. Workflow diagrams for the modeling of (a) the above-diurnal filter and (b) the daily filter. (a) The above-diurnal filter workflow consists in (a1) the pre-processing involving the secular trend removal, (a2) the predefined processes and the neural network modeling, and (a3) the post-processing involving adding the secular trend back. (b) The daily-filter workflow consists in (b1) the computation of the summed diurnal component, (b2) the predefined processes and the neural network modeling, and (b3) the computation of modeled output. The modeled outputs from (a3) and (b3) are finally added together in (c) to compute the final modeled outputs.

To test whether the LSTM neural network could model the filter data, we set up experiments to search for an optimum number of neural network layers. Using the $f_{>24}$ variation excluding the secular trends as the output targets and solar wind and geometrical data as the input features (see Section 4.1), we find that using five hidden layers as displayed in Fig 1 provides reasonable modeling results in comparison to the observed data. Technically, this type of artificial neural networks is called "deep neural networks", but we will simply call them neural networks in the rest of the paper for short. To avoid overfitting, we add a dropout layer, which helps to generalize the results (Srivastava et al., 2014), with a dropout ratio of 0.2. The number of hidden parameters in the first layer is chosen to be 100; the numbers of hidden parameters in the second, third, fourth, and fifth layers are chosen to be 50. We tried smaller numbers of the hidden parameters in our early attempts; the numbers specified here provide rather satisfactory results (see Section 4). The final neural network architecture is summarized in Fig 1.

For the model training, we set up the neural network to learn in batches where it learns from a certain amount of data at a time. Here, the batch size is set to 256 for the training data at 1 hour cadence (95,945 data points for the data in 1997 - 2007). The weights and biases in the neural network layers and nodes are updated through several cycles. The number of training cycles is known as "epoch". The learning process is optimized and tracked through the loss function, which evaluates the model performance during each training epoch. Here, the loss function is set to be the mean squared error. We monitor the learning process through the validation loss (see Section 3.2). The learning process is stopped once there is no improvement in the validation loss for five con-

secutive epochs. The best model is saved when the validation loss reaches a minimum value before the training stops. Furthermore, we set the optimization algorithm to be "Adam" (Kingma & Ba, 2014) with the learning rate of 0.001. These setups proved to work reasonably well for our filter data as will be shown in the Section 4.

3.2 Neural network training: the walk forward approach

To effectively train the neural network model, we split the datasets, comprising the solar wind and solar radio flux, the geometrical parameters, and the filter data, as the following. Overall, we split the sequential data into the training, validation, and test sets. The validation set is used for evaluating and monitoring the model performance during the learning over several epochs. The ground magnetic measurements have temporal dependencies coming from the solar wind and solar dynamo (influencing the solar activities or phases). Therefore, the choice of training and validation data can introduce biases. Firstly, the neural network must be trained using a sufficient amount of data, in this case a complete solar cycle, so that it learns more or less from all the possibilities. Secondly, since a best model is chosen based on the validation data, the choice of validation data can also introduce a bias. For example, if the model is validated and selected using an interval of data with active solar activities, i.e., during a solar maximum where the occurrence of ICMEs is high, the model may not be appropriate for use during the quiet solar activities, i.e., during a solar minimum where the occurrence of ICMEs is low. To minimize such a bias, we propose a new strategy for the model training as follows.

To best capture the different nature of solar activities in the various phases of the solar cycle, we propose an adaptive training method called "Walk Forward Validation" (also called "Sliding Window" or "Rolling Forecast") approach (e.g., Brownlee, 2019). A schematic illustration is shown in Fig 3. This approach has been used in economy and stock market predictions where the model is retrained once newer data become available (e.g., Kaastra & Boyd, 1996). The advantage is that the model would be the most up-to-date, making it more relevant to the current situation and thus the near future situation. In brief, the model is trained in several steps while moving forward along the time series. The walk forward approach can be summarized as follows.

1. The model is trained with the data within a specified minimum training window (Fig 3a) as shaded in blue. It is then validated with the unseen data adjacent to the training data defined within a specified validation window as shaded in green.
2. The model is trained again with the data in a next, shifted training window (Fig 3b). The validation data in the previous step are included in the training data. The model is then validated with the unseen data, defined within a specified validation window, adjacent to the newly shifted training window.
3. The process is repeated until the end of all the training data (Figs 3a - 3c) excluding the test set (Fig 3d) as shaded in purple.

For our purpose, we define a minimum training window to be 11 years and a validation training window to be one year. Data in 2009 and 2012 are taken as the test datasets representative of the quiet and active solar periods, respectively. Since the high-resolution OMNI data are only available from 1995, we perform the walk forward training from 1995 up until 2009 (with data in 2008 being the validation data in the last training step, see Fig 3) and 2012 (with data in 2011 being the validation data in the last step). Here, the model is most relevant to the time closer to the end of the training window as it is trained several times using the newer data, while being less relevant to the older data. This approach would offer optimum results for the time-dependent prediction made by the neural network. We demonstrate the performance of the walk forward training in the SI.

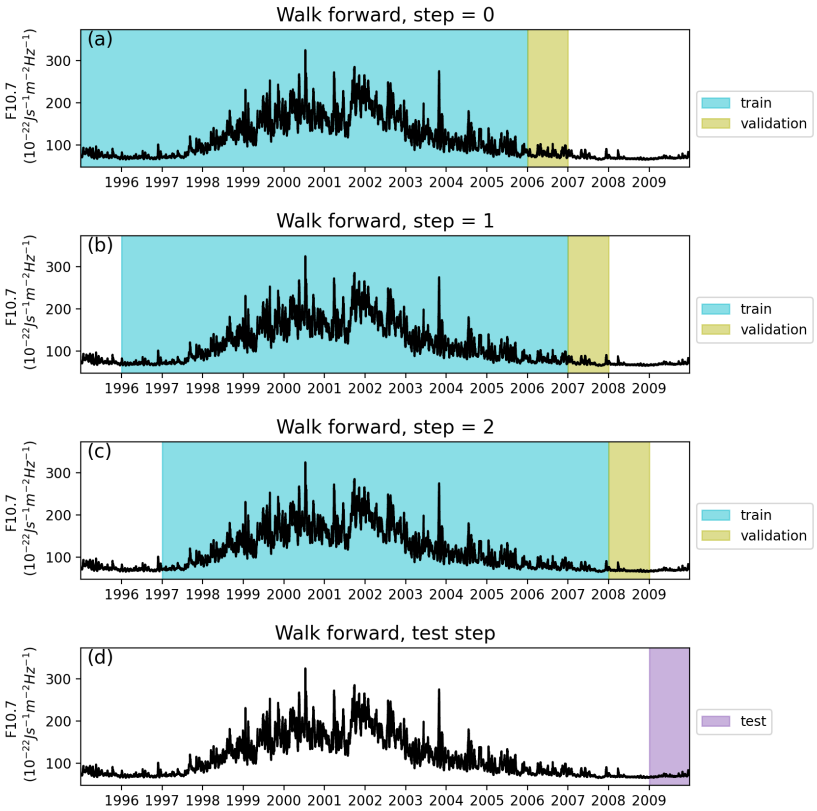

Figure 3. The walk forward training approach. The F10.7 (black) indicative of the solar variability, i.e., the solar cycle phases, is shown for context. (a - c) The walk forward approach consists in several training and validation steps leading up to the test year, here shown for 2009. (d) The model is tested after the final training and validation step.

4 Results

Here we report our modeling results from the neural networks using the walk forward training described in Section 3 for quiet (2009) and active (2012) solar activity periods. We start by presenting the model results for the $f_{>24}$ in Section 4.1 and then for the f_D in Section 4.2. The final outputs, $f_{>24}$+f_D, are then presented in Section 4.3. Finally, we present the results using the same neural networks but with restricted independent parameters to model the quiet variation, i.e., geomagnetic baseline, in Section 4.4.

4.1 Modeling of the above-diurnal ($f_{>24}$) contribution

The $f_{>24}$ data are shown in Fig 4. From Haberle et al. (2022), the $f_{>24}$ is dominated by the secular variation due to the change in the main field at the location of the ground station. Particularly, the Earth's south magnetic pole, locating in the geographic north, was found to have drifted from its location in the Canadian arctic, determined from the first in-situ measurements in 1831, towards Siberia (Olsen & Mandea, 2007; Livermore et al., 2020) over the past decades. Consequently, the magnetic measurements at CLF in Europe shown in Fig 4 remarks a steadily increasing trend in all magnetic components, in the order of tens of nanotesla (nT) per year. This secular trend dominates over the variations coming from other sources and it was estimated to constitute 93% of the overall measurements in magnitude. To model the $f_{>24}$ contributions owing to the

solar-driven perturbations, we consider a pre-process of the data by removing this secular trend. In brief, we removed this trend by subtracting the 30-day running average of the $f_{>24}$, denoted as $\langle f_{>24} \rangle_{30D}$ as shown in Fig 4 for all magnetic components in orange, from the original $f_{>24}$ data. Appendix A describes our process for this choice in detail.

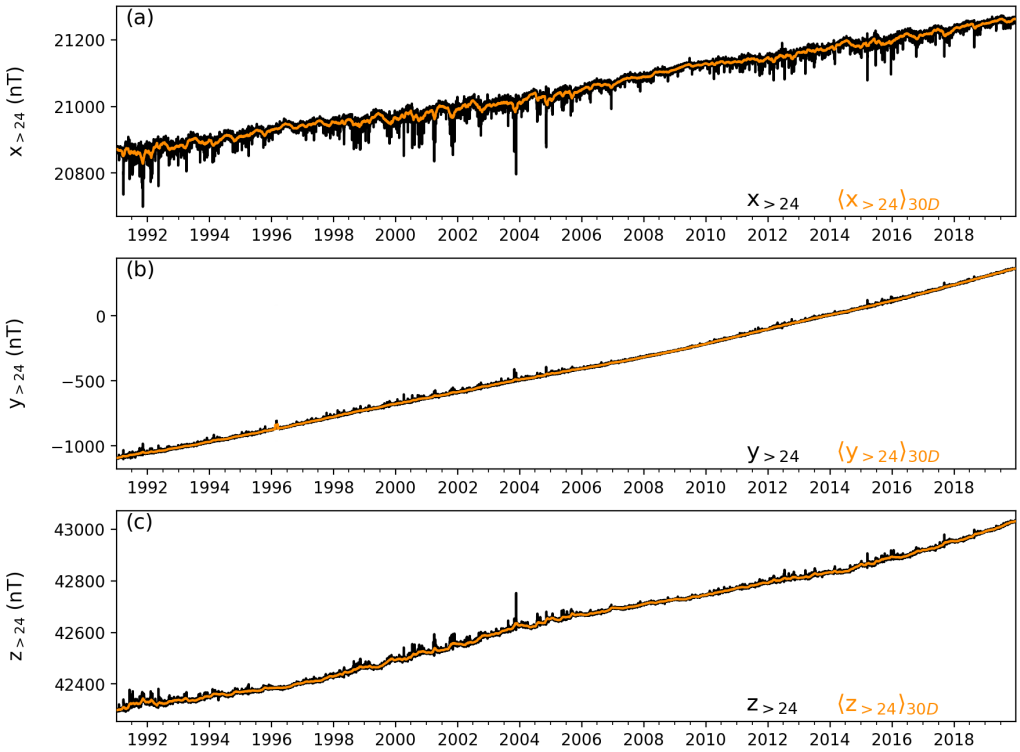

Figure 4. Above-diurnal ($f_{>24}$) variations of the ground magnetic measurements at Chambon-la-Forêt (CLF) between 1991 and 2019 (black) and their 30-day running averages (orange) shown for the x, y, and z components in panels (a), (b), and (c), respectively.

We now focus on qualitative results. Here, the detrended $f_{>24}$ are taken as the output targets (see Fig 1) of the neural network. The modeling results are rescaled to the original units (nT) and the removed trend at the pre-processing step is added back at the post-processing step (see Fig 2a). Fig 5 shows data in 2009 and 2012 in left and right panels, respectively. The solar wind speed and the IMF B_z along with their 24-hour running averages are shown in panels (a, f) and (b, g) for the context. The comparison between the observed data (black) and the modeling results (red) is shown in other panels. Considering the $f_{>24}$, there is an overall agreement for the trend and smaller-scale fluctuations for both 2009 and 2012. There are several peaks and dips, especially in the $x_{>24}$ component, in addition to the secular variation. These occasional drops in $x_{>24}$ and peaks in other components correspond to the perturbations due to ICMEs and high-speed stream arrivals (caused by CIRs), in some cases in conjunctions with negative IMF B_z especially in 2012. At these peaks and dips, there are some apparent mismatches in the strength at peak values visible in all components. At around July - September 2009, for instance, there are clearly a few local dips in the $x_{>24}$ component where the minima of the modeled data are lower than those of the observations. Meanwhile, at around July - August 2012, these peaks appear to be overestimated. Furthermore, there is a slight

gap, i.e., a relatively small offset, between the observed and modeled (average) values in the last three months of the year for both 2009 and 2012, best seen in Fig 5c. This offset is due to the trend removal process; this aspect is discussed in Section 5. Despite the offset, our results demonstrate an overall good agreement with the original $f_{>24}$.

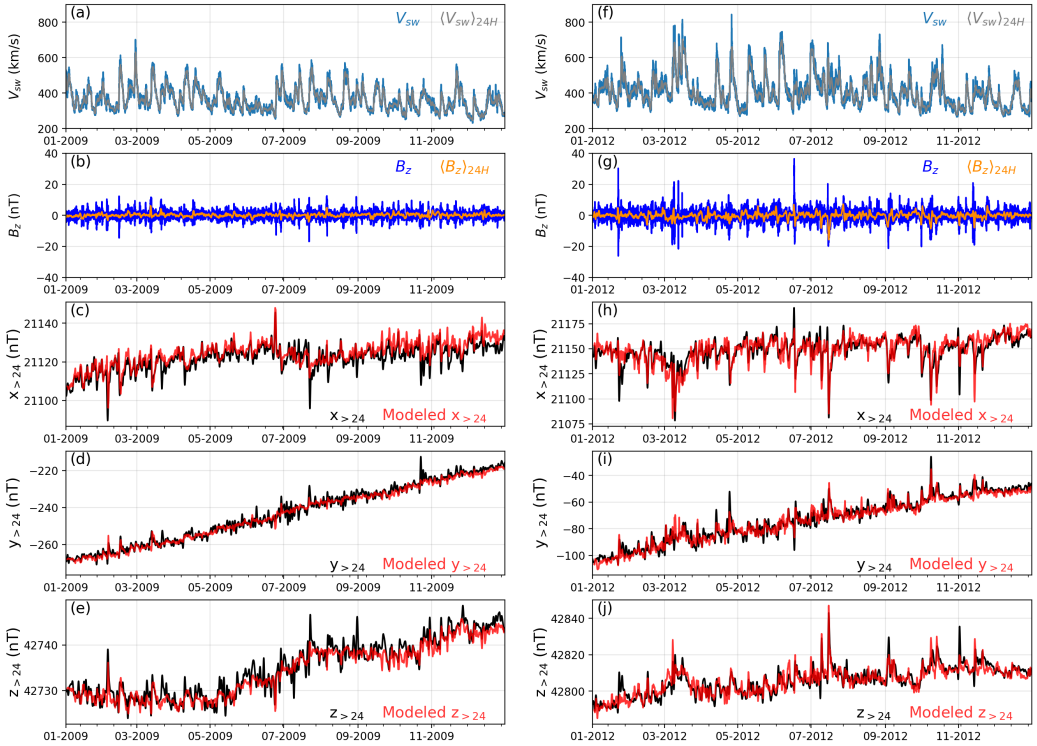

Figure 5. Solar wind speed (a, f), IMF B_z (b, g) and a comparison between the original $f_{>24}$ (black) and the modeling results (red) shown for (c, h) $x_{>24}$, (d, i) $y_{>24}$, and (e, j) $z_{>24}$ components in 2009 (left) and 2012 (right). The solar wind speed and IMF B_z are shown for context along with their 24-hour running averages used as inputs for the model.

4.2 Modeling of the daily contribution

In this Section, we consider the daily filter f_D that is the sum of filters f_{24}, f_{12}, f_8, and f_6 of the ground magnetic measurements. Physical contributions to these individual filters are discussed in Haberle et al. (2022). In brief, the f_D captures the Sq current systems including their day-to-day variability at mid-latitude, which show significant dependencies on the neutral atmosphere including neutral winds and tides. Using the same inputs as for the $f_{>24}$ (Section 3.2), we test whether the neural network can model the f_D. Specifically, we use the same neural network architecture but change the output targets to be x_D, y_D, and z_D as summarized in Fig 2b.

4.2.1 Daily contribution: solar-quiet year

Fig 6 shows a comparison between the original $f_D = (x_D, y_D, z_D)$ and the modeling results for 2009. A winter month (February, a-c) and a summer month (August, d-f) were chosen for displaying the results. The original f_D (black) shows daily, periodic variations that are almost regular particularly for y_D and z_D. These regular variations may indicate that they are mostly modulated by the geometrical parameters. The orig-

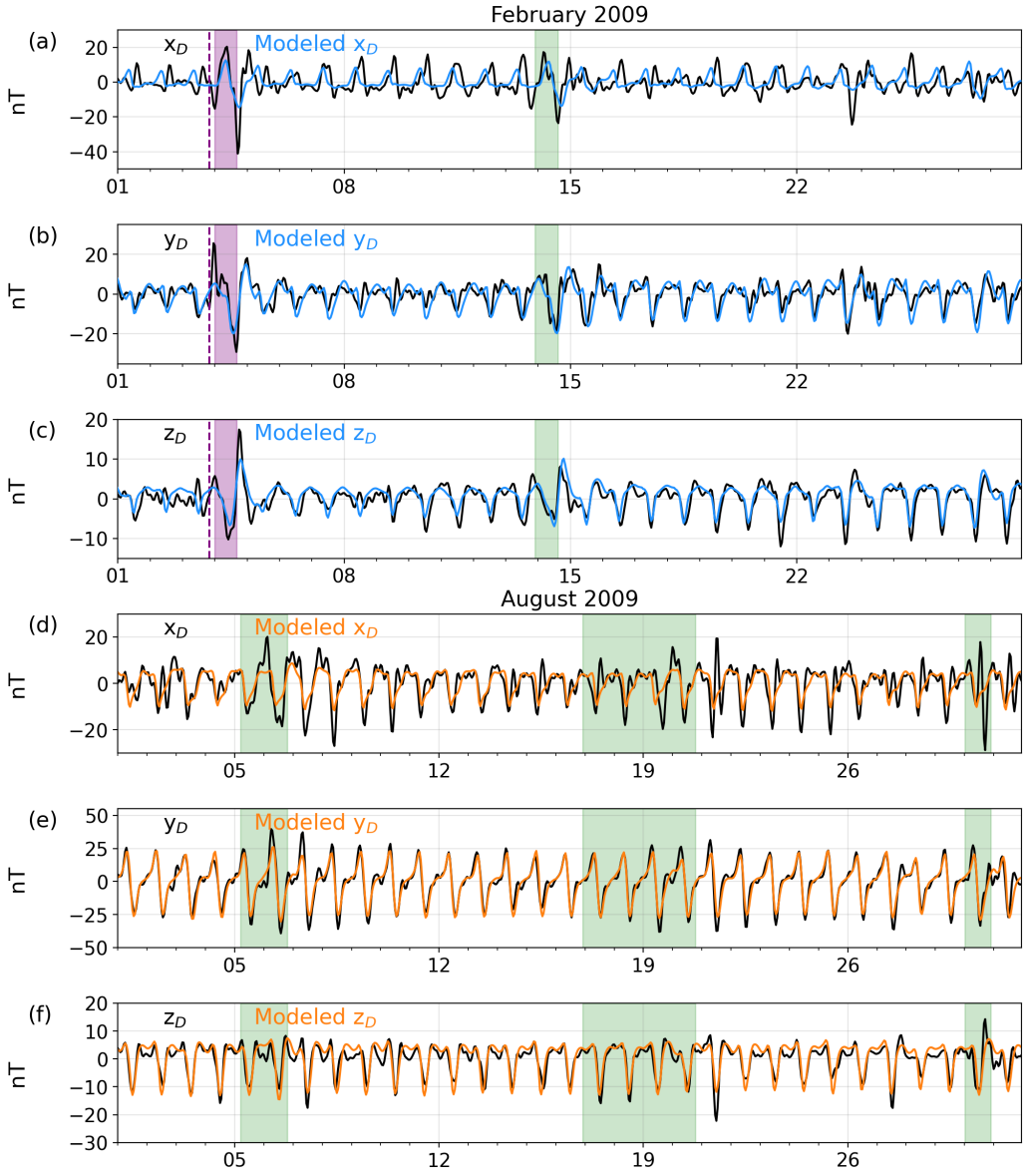

Figure 6. Comparison of the original data (black) and the modeling results for the daily filter (f_D) for a winter month (February; a-c) and a summer month (August; d-f) in 2009. The modeled x_D, y_D, and z_D are shown respectively in panels (a - c) for February in blue and in panels (d - f) for August in orange. Purple and green shades highlight the intervals of ICME and CIR passages, respectively. A purple vertical dashed line marks the beginning of ICME disturbances.

inal x_D, however, shows less regular periodic variations. Our modeling results show excellent agreements for y_D in August, shown in orange. To the first order, our neural network model produces similar periodic variations to the original f_D, especially in August where the amplitudes of the daily variations are stronger. To the second order, however, there appear certain extrema of the variations (e.g., Fig 6e) in which our modeling results underestimate their peak values. Furthermore, there are smaller-scale variations, which appear as secondary bumps in between the daily extrema in all components. Importantly, in February, our model produce daily variations that appear to be slightly out-of-phase as can be seen in Fig 6b. This effect is less strong for z_D (Fig 6c) except for the first week. Meanwhile, the results are relatively poorer for x_D (Figs 6a, 6d) where some observed peaks are missed completely. Here, the X-direction corresponds to the geographic north. With CLF being at mid-latitude, the x components ($x_{>24}$, x_{24}, etc.) could be influenced by the perturbations coming from the higher latitudes such as the auroral electrojets as well as from the lower latitudes such as the equatorial electrojets. In brief, the x_D is more susceptible to perturbations of solar origins (this effect is different at various geographical latitudes). Apart from the issues with the x_D, our neural network results show good qualitative agreement with the observed y_D and z_D.

We now focus on apparent perturbations in the different months. In February 2009, apart from the regular periodic variations, there are clear perturbations in the original data, e.g., around February 4 - 5, in all components. These fluctuations are the perturbation following the passage of an ICME on February 4, from 00:00 to 16:00 UT (see the ICME catalog by Richardson & Cane, 2010). We highlight this interval in purple shade as well as for the arrival of the ICME disturbance (i.e., shock) with a purple dashed vertical line. This ICME disturbance caused the daily extrema to be further driven, appearing as strong peaks and dips, in all components. It is apparent that the modeled signals (blue) underestimate these peaks, especially for x_D. Furthermore, we mark a passage of the CIR on February 14th in green shade (see the updated catalog by Jian et al., 2006). This CIR arrival caused the original f_D to dip further than the previous days. Our model underestimates these dips for all components, especially for x_D. In August 2009 (Figs 6d - 6f), there appears nearly a week-long perturbation between August 5 and 11. These perturbations follow the CIR passage between August 5 ∼04:45 and August 6 ∼19:15 as marked in green shade. From Jian et al. (2006)'s list, it was marked that there is an ICME embedded in this CIR. Our model (orange lines) again underestimates the peaks, in particular for x_D and y_D. Additionally, there are two more CIR passages in the same month as highlighted in green, although their effects are less clear. In brief, we find that our model results reproduce the daily variations rather well although they reproduce less well the perturbations induced by the passage of solar-transient structures.

Overall, the modeling results appear better for August. Among the three components, the neural network performs less well for the x_D component. We conclude that our neural network for the daily filter f_D performs rather well for the solar-quiet period.

4.2.2 Daily contribution: solar-active year

We now consider a solar-active year. Fig 7 shows a comparison between the original data and the modeling results for 2012 for a winter month (January; a-c) and a summer month (July; d-f). We note that our model results are available from January 2 at 06:00 onwards because it takes 30 hr history of the data (starting from January 1 at 00:00) for the LSTM neural network to produce one data point. The original signals (black) show stronger amplitudes of the daily variations compared to those in 2009 in general. There are two ICME arrivals in January 2012; the first one is between the 21st at ∼06:00 and the 22nd at ∼ 08:00, the second one is between the 22nd at ∼23:00 and the 23rd at ∼ 07:00 UTC as highlighted in purple shades. We find that the neural network model underestimates the perturbations in all the components, especially for x_D. In addition,

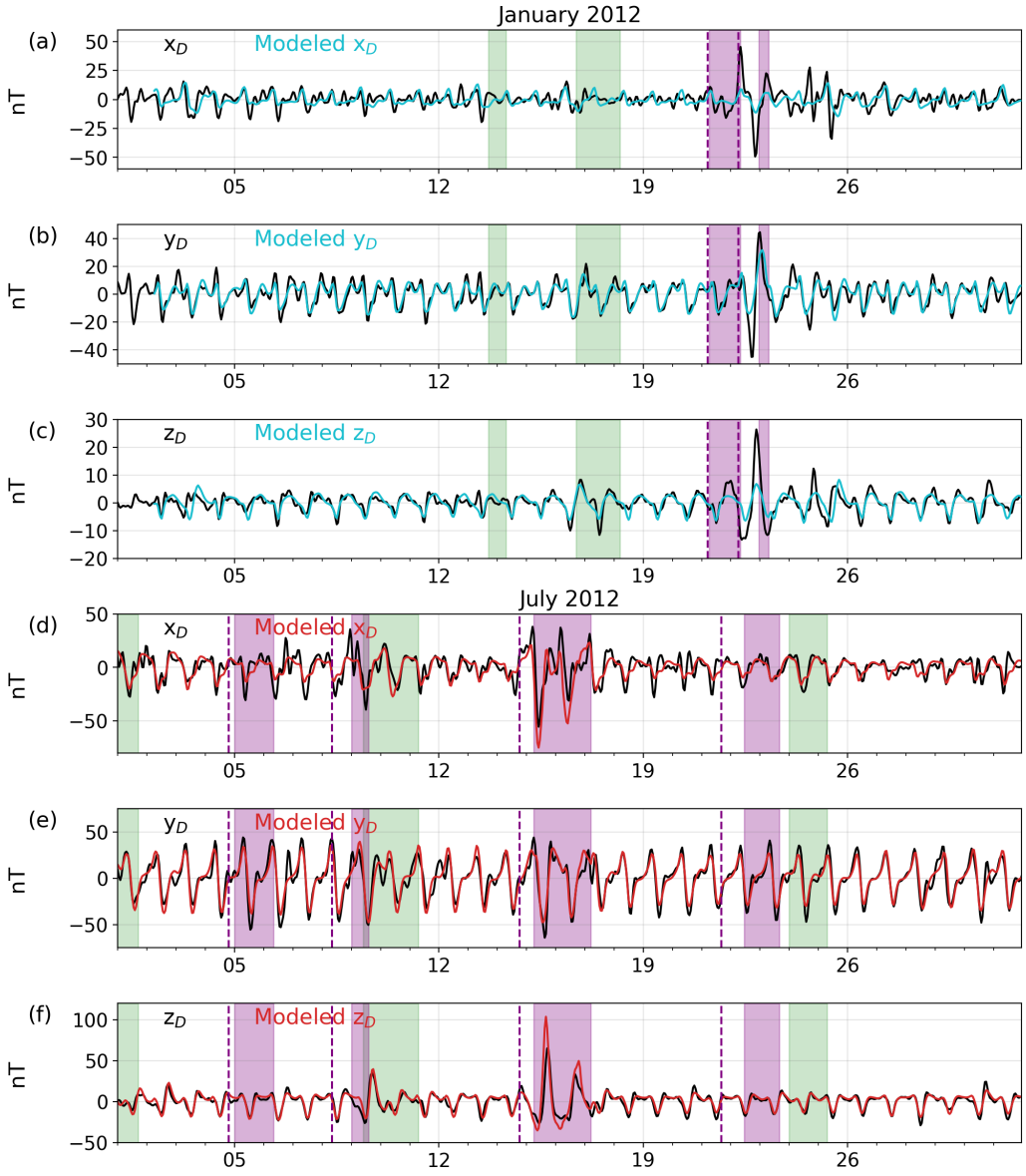

Figure 7. Comparison between the original data (black) and the modeling results for the daily filter (f_D) for a winter month (a-c) and a summer month (d-f) for 2012. The modeled x_D, y_D, and z_D are shown respectively in panels (a - c) for January in cyan and in panels (d - f) for July in red. Purple and green shades highlight the intervals of ICME and CIR passages, respectively. Purple vertical dashed lines mark the starting times of ICME disturbances.

there are two CIR passages as highlighted in green shades. Our model replicates the observed variations rather well although the extrema are underestimated.

We now focus on storm perturbations. In July 2012 (Figs 7d - 7f), there are four ICME arrivals on the 4th, 8th, 14th, and 21st (see the catalog by Hajra & Sunny, 2022) as marked by dashed purple lines. The time intervals of these ICME passages are highlighted in purple shades. Among these four ICMEs, only the one arrived on July 14 appears to induce strong perturbations especially in x_D and z_D. Based on the properties of those ICMEs, the one arrived on the 14th has the fastest average bulk flow speed (490 km/s) and the fastest maximum bulk flow speed (670 km/s) compared to the others which are in the range of 310 - 540 km/s for both quantities. Our model (red solid lines) appears to reproduce and somewhat overestimate the perturbation peaks seen in x_D and z_D in this case, albeit the slight underestimation for y_D peaks. In addition, there are a few CIR passages as shaded in green although there appear no clear perturbations on the f_D. We will further discuss the effects of ICMEs and CIRs in Sections 4.3 and 5. Overall, the neural network reproduces some of the storm perturbations in addition to the daily variations for 2012 although the extrema are often underestimated.

4.3 Final modeling results: the filter baseline

We have now modeled both the $f_{>24}$ and the f_D filters. Next, we consider a sum of these two modeled signals in order to produce our final output product (Fig 2c). The sum of the filters, namely $f_{>24} + f_D$, was proposed by Haberle et al. (2022) to be a geomagnetic baseline during magnetically quiet periods. We define this as a filter baseline (f_{FB}). This baseline was compared to existing baselines such as those from the FMI and SuperMAG. We focus first on the ability of the neural networks to reproduced the original f_{FB}. We will then consider the production of a geomagnetic baseline by excluding the non-quiet variations owing to the solar wind and IMF in Section 4.4.

4.3.1 Modeling of the filter baseline: solar-quiet year

Fig 8 shows the results for February (a - c) and August (d - f) 2009, similar to Fig 6 with the highlighted ICME (purple shade) and CIR (green shade) passages. We find that our modeled $f_{FB} = (x_{FB}, y_{FB}, z_{FB})$ shows overall good agreements especially for y_{FB} and z_{FB} in the absence of perturbations owing to the solar transients, e.g., between August 10 and 16 in Figs 8e and 8f. Similar to Section 4.2.1, we find some mismatches for the extrema and small-scale features. The f_{FB} in February shows poorer agreements with the original f_{FB}, especially for x_{FB} and z_{FB} where there is a slight gap or a small offset between the observed and modeled data, best seen in Fig 8a in the first week. The f_{FB} in August (Fig 8d) shows a better qualitative agreement with the observations. During and after the ICME passage highlighted in purple (Figs 8a - 8c), our model underestimates the extrema. In the presence of CIR perturbations highlighted in green, our model results mostly show an underestimation of the daily extrema, consistent with the results in Section 4.2.1. Additionally, we evaluate the performance by computing the Pearson correlation coefficient (Pcc) and R^2 score in Appendix B for each month in 2009 (see Table B1). We find that the average Pcc and R^2 score values are better in summer than in winter. The average of the monthly Pcc and R^2 score values for 2009 are found to be [0.62, 0.87, 0.81] and [0.14, 0.70, 0.65], respectively, for the (x_{FB}, y_{FB}, z_{FB}) components. The average Pcc and R^2 values of the three components are 0.77 and 0.49, respectively.

4.3.2 Modeling of the filter baseline: solar-active year

Fig 9 shows the results for January (a - c) and July (d - f) 2012, similar to Fig 7. Note that the modeling data start from January 1 at 06:00 only as it takes 30 timestamps starting from January 1 at 00:00 to produce the first points. Outside the perturbed periods (non-shaded intervals), our model shows rather good agreements for y_{FB} and z_{FB}.

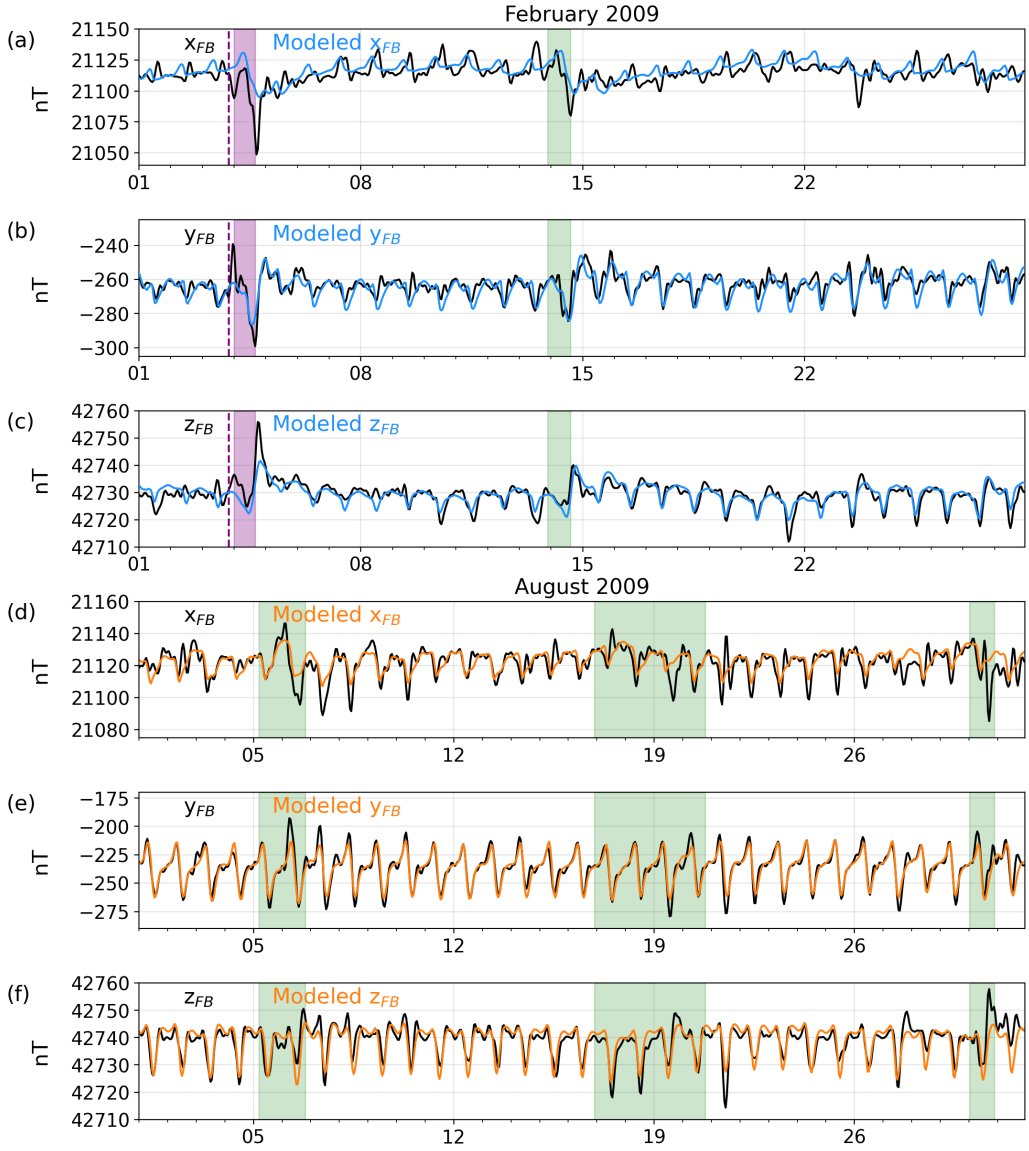

Figure 8. Comparison between the original filter baseline (f_{FB}, black) and the modeling results for 2009 shown for February (a-c) and August (d-f). The modeled signals are in blue and orange for February and August, respectively. Purple and green shades highlight the ICME and CIR passages, respectively. A purple dashed line marks the ICME disturbance.

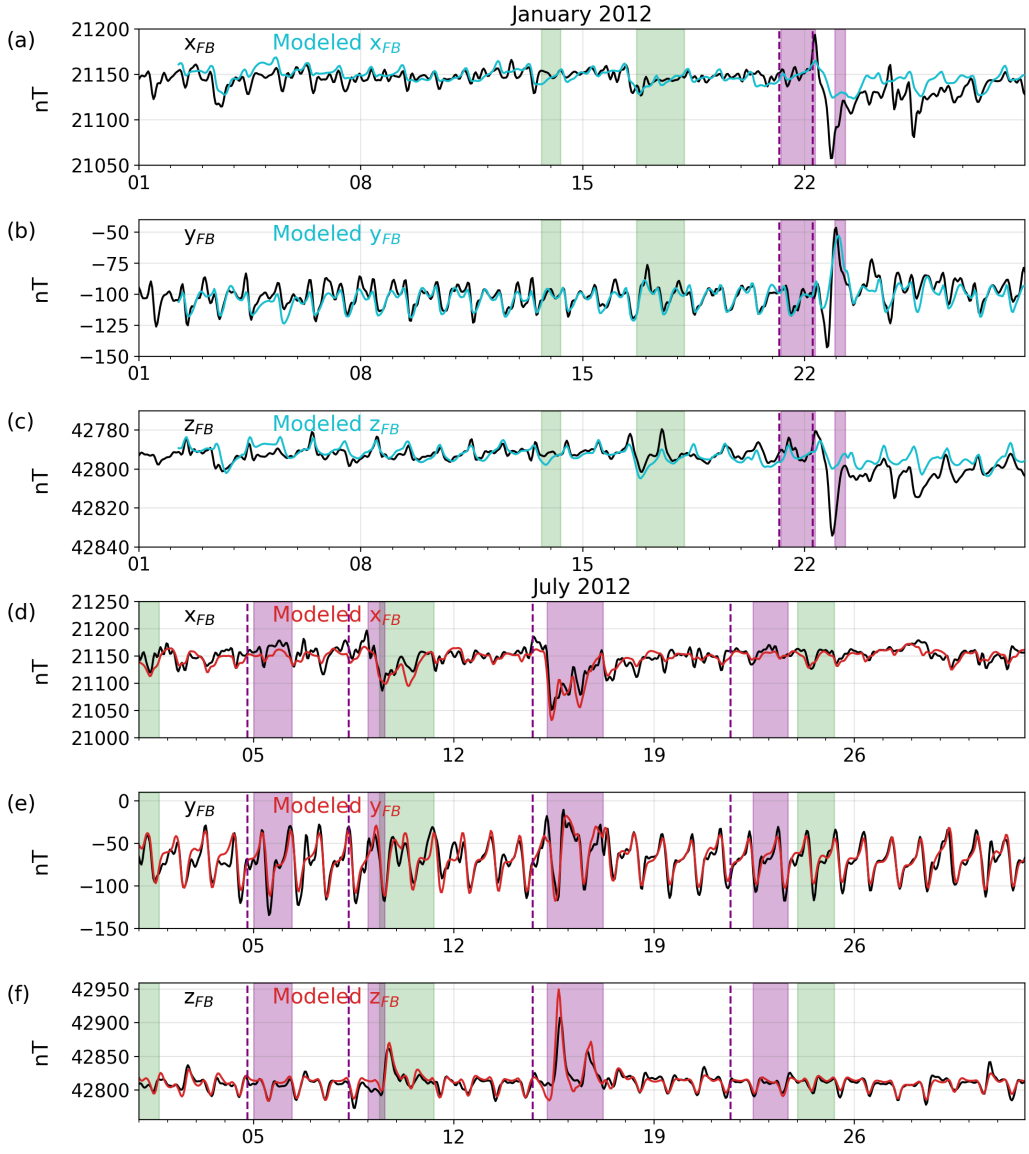

Figure 9. Comparison between the original filter baseline (f_{FB}, black) and the modeling results for 2012. The modeled signals are shown in cyan for January (a - c) and in dark red for July (d - f) for x_{FB}, y_{FB}, and z_{FB}. Purple and green shades highlight the ICME and CIR passages, respectively. Purple dashed lines mark the beginning of ICME disturbances.

In the presence of ICME passages (purple shades), the original f_{FB} (black) show strongly perturbed variations especially between January 21 and 26, and between July 14 and 18. For the ICME in January, it is apparent that the perturbations on the filtered ground magnetic measurements persist up to a few days after the ICME arrivals and passages. Our model underestimates its effects for the x_{FB} and y_{FB} while showing some reproduced peaks for the y_{FB}. The CIR passages (green shades) in the same month produce barely noticeable effects. In July 2012, there are several ICME and CIR passages with variable visible effects on the original f_{FB}. The strongest effect is visible between July 14 and 18 as mentioned earlier. Our model correctly produced the perturbations in all components, despite some overestimation in x_{FB} and y_{FB}. Similar to the solar-quiet year, our modeling results have better quantitive results in summer than in winter (see Table B2 in Appendix B). The average of the monthly Pcc and R^2 score values are found to be [0.76, 0.90, 0.83] and [0.51, 0.79, 0.65], respectively, for the [x_{FB}, y_{FB}, z_{FB}] components. The average Pcc and R^2 values of all the three components for 2012 are found to be 0.83 and 0.65, respectively, which are better than those in 2009.

Overall, we find that our approach produces rather similar results to the baseline from Haberle et al. (2022). However, there are somewhat dissimilar results in the presence of perturbations owing to the solar transients, and some disagreement in the x_{FB}. We will discuss future improvements and applicabilities of our approach in Section 5.

4.4 Neural network modeling of the quiet variations

We now consider the modeling of the quiet variations within the filter data in an absence of the external drivers, i.e., the solar wind and IMF. The aim is to be able to produce a geomagnetic baseline representative of the regular variations modulated solely by the quiet sources using the neural networks for both quiet and active solar periods. The quiet, regular variation is dominated by the solar-quiet (Sq) variation which yields the day-to-day variation (24 hr period) measurable at a ground station. The Sq variation is produced by the recurring ionospheric current on the sunlit side under which the station rotates. Thus, the F10.7 indicative of the solar irradiance and the local time are useful parameters. Furthermore, this Sq variation varies depending on the season. To take into account the quiet variation, we thus build a similar LSTM neural network as in Section 3 but with the input parameters being only the F10.7, SZA, and LT. This neural network is to model the daily filter f_D. Since the quiet variation of the $f_{>24}$ is the secular variation of the Earth's internal magnetic field, we can indeed take only its running average (30-day) to represent its quiet contribution. Finally, the total quiet variation is the sum of the 30-day running average of $f_{>24}$ and the modeled f_D without the solar wind and IMF. We name this product as $f_{FB,noSW} = \langle f_{>24} \rangle_{30D} + f_{D,noSW}$.

Fig 10 shows a comparison between the original filter baseline f_{FB} from Haberle et al. (2022) and the neural network filter baseline when excluding the solar wind and IMF ($f_{FB,noSW}$), as shown in black and red, respectively. Panels (a) - (c) show the x, y, z components in August 2009. We find that the $f_{FB,noSW}$ shows periodic variations similar to the original f_{FB} for all components with the amplitudes being correctly reproduced. The y-component, in particular, shows an excellent agreement during quiet time, e.g. between August 12 and 19. The x- and z-components, however, show an agreement to a lesser extent. Importantly, in the presence of the perturbations appearing in the original f_{FB} as shaded in green for CIRs and in purple for ICMEs, e.g. between August 5 and 12 driven by the CIR, our $f_{FB,noSW}$ remains regular. This is a desirable quality of the geomagnetic baseline that robustly represents the quiet variation without being sensitive to the external drivers. Panels (d) - (f) show the x, y, z components in July 2012. In the presence of the perturbations, e.g., between July 14 and 20 driven by the ICME, the modeled $f_{FB,noSW}$ also remains regular. The same results yield for winter 2009 and 2012 months (not shown). This shows a potential applicability of the $f_{FB,noSW}$

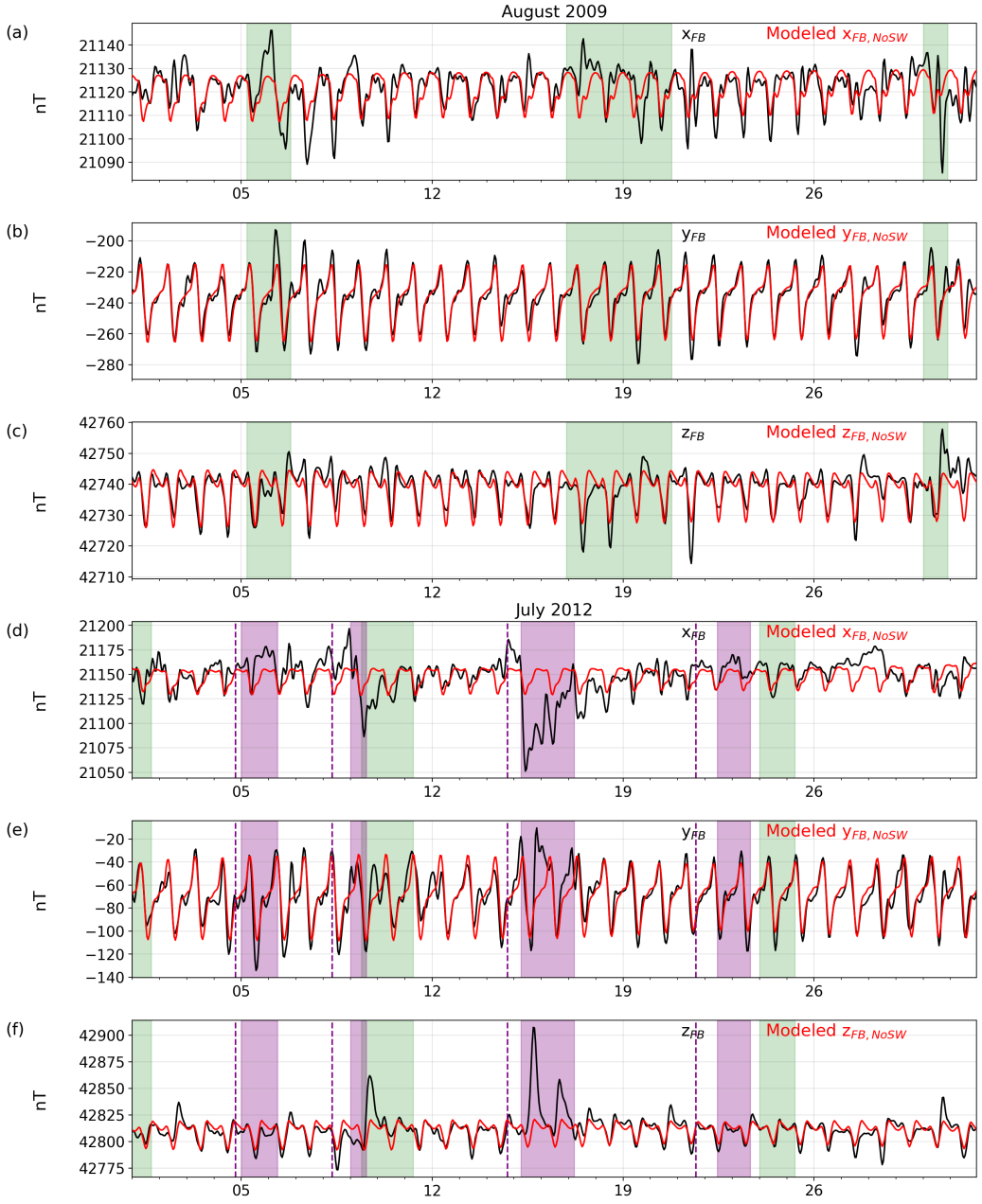

Figure 10. Comparison between the original filter baseline $F_{FB} = (x_{FB}, y_{FB}, z_{FB})$ (black) and the modeled filter baseline when excluding the solar wind and IMF $F_{FB,noSW}$ (red). The data are shown for August 2009 (a - c) and July 2012 (d - f), for the x- (a,d), y- (b,e), and z- (c,f) components. Green and purple shades highlight the CIR and ICME passages, respectively. Purple dashed lines mark the beginning of ICME disturbances.

as a geomagnetic baseline that would robustly represents the regular variation for both quiet and perturbed periods.

5 Discussion

We have modeled the above diurnal ($f_{>24}$) and the daily (f_D) variations of the geomagnetic baseline derived using the filtering technique proposed by Haberle et al. (2022). Our purpose is to be able to reproduce these variations using neural networks. Using the in situ observations of the solar wind IMF and plasma parameters, the daily F10.7 cm solar radio flux, and the geometrical parameters as inputs, we built the neural networks to model $f_{>24} = (x_{>24}, y_{>24}, z_{>24})$ and $f_D = (x_D, y_D, z_D)$ at 1 hr cadence. The LSTM architecture was chosen in order to be able to account for the history of the observations which may contain the solar wind perturbations and/or the solar transients in the last 30 hours. Using data from 1995 onwards, we developed individual neural networks for $f_{>24}$ and f_D using the walk forward training (Fig 3). The data in 2009 and 2012 were chosen as the test data for a solar-quiet year and a solar-active year, respectively.

Our neural network is illustrated in Fig 1 where it comprises five hidden layers; this neural network is identical for $f_{>24}$ and f_D. For $f_{>24}$, we first removed the secular trends owing to the change of the internal geomagnetic field before feeding them into the neural networks; the removed trends were then added back at the post-processing step (Fig 2). We then considered the sum of $f_{>24}$ and f_D, the so-called f_{FB}, as our final modeled product. We find that our approach produces $f_{>24}$ and f_D, and subsequently f_{FB}, agree qualitatively well with the original signals. The yearly averaged Pcc of the modeled [x_{FB}, y_{FB}, z_{FB}] was found to be [0.62, 0.87, 0.81] for 2009 and [0.76, 0.90, 0.83] for 2012. (see Appendix B). In the presence of perturbations following arrivals and passages of solar transients including ICMEs and CIRs, however, our approach produced more arbitrary results where peaks of the perturbations are underestimated or overestimated depending on the component and/or the event, although the overall shape of the signal is preserved. In general, we find that the model results are better in summer. This is plausibly because the amplitude of the daily variations is stronger, making it more discernible and thus easier to model. Besides, we find that the results in 2012 are better, plausibly for the same reason as the fluctuations are stronger during a solar-active year compared to a solar-quiet year. We conclude that our approach provides good agreement to the f_{FB} proposed by Haberle et al. (2022) for both solar-quiet and solar-active periods.

We discuss some caveats of our approach as the following. First, the secular trends in $f_{>24}$ were removed using the rolling average with a window of 30 days. This trend removal process was aimed to get rid of the secular variation of the geomagnetic field measured at CLF; this process also helps the neural network to be able to learn patterns owing to the perturbations of solar origins. Nevertheless, the rolling average may also remove some useful information. In particular, some large-amplitude perturbations owing to the effects of solar-transient structures can also be partially removed. As a consequence, the data we fed into the neural network underestimate the actual magnitude of the perturbations. This plausibly explains the underestimation of extrema during the storm-perturbed fluctuations predicted by our neural network. It would be desirable if we can remove this secular trend based on physical understandings. The use of main geomagnetic field model outputs together with constants on each component, to take into consideration the local crustal biases at the considered magnetic observatory location, will likely reduce the observed discrepancies between the filter data and the neural network model results. The IGRF model (International Geomagnetic Reference Field; Alken et al., 2017), for instance, in conjunction with constant values to consider the crustal field due to remnant rocks within the crust may be considered in our future improvements. Yet, this approach will downgrade the capacity of real-time calculation and lead to use of a priori information, making it less convenient for operational implementation.

Our model shows less satisfactory results for $x_{>24}$, x_D, and subsequently x_{FB}, unlike for other components. This is likely because the x-component is influenced by the solar and geometrical parameters differently unlike the y- and z-components. Since CLF is at mid-latitude, the x-component which records fluctuations in the north-south direction can be influenced by both the auroral electrojets from high latitudes and the equatorial electrojets and ring currents from low latitudes. Technically, the x-component may be modeled separately using a dedicated neural network, and this will likely improve the model performance. However, the x-component is indeed a projection of a physical (vector) quantity — the magnetic field — that cannot be treated apart. Overall, we find that our current configuration provides reasonable results; it demonstrated that the machine-learning based model can be used. Future work should include an optimization of this approach for yielding better results.

Our work focused on the effects of solar-driven perturbations on the filter baseline. Despite that, there may be other important drivers of inner-magnetosphere origins and/or atmospheric origins that should be taken into account. For example, even if this current modeling attempt reproduces reasonably well the day-to-day variability, atmospheric gravity or tides may have other measurable effects at the ground level. Currently, we do not have exploitable measures that can be fed into our model at the time of our model development. It would be desirable to understand or identify all sources relevant to the magnetic measurements at the ground level. Progress in this field of research would potentially improve our future modeling. Importantly, since we take the solar wind IMF and plasma data upstream of the Earth, we bypass the understanding of the coupling of various physical processes in the magnetosphere down to the ground. Our approach does not give any physical insights; it merely provides an advanced statistical machine-learning based model. Exploring the transparency of machine-learning based models is currently an active area of research. Investigation of interpretability (e.g., Lundberg & Lee, 2017) of the neural networks may provide physical insights and improve our understanding.

We demonstrated the applicability of the neural network modeling in predicting the filter baseline. Particularly, we demonstrated that the neural network can model the regular, quiet variation when excluding the solar wind and IMF. Although we focused on data from CLF, our approach is scalable and can be applied to data from other stations. Future applications of our approach include (a) producing a machine-learning based geomagnetic baseline, and (b) predicting the solar-driven ground magnetic measurements. For (a), we need more analyses to test the robustness of our modeled quiet variations driven by the solar irradiance and the geometrical parameters. A test for producing the quiet variations was performed; it showed promising results as demonstrated in Section 4.4. For (b), we will need future improvements for predicting more accurate results for the x-component, as well as further validation and extension of data interval for the model training to cover the various phases of a solar cycle. Importantly, the impacts of CIRs and ICMEs should be assessed. This work is a proof of concept that the neural network can be used for predicting ground magnetic perturbations driven by the solar wind. Our method can be adapted for real-time use. Once the neural networks are trained with sufficiently long data (e.g., two solar cycles), they can be retrained every month or every day to update the models and then make forecast for the next month or next day(s).

In terms of the computational resources, our approach is rather efficient. For the model training part with the walk forward training, it takes 1 hour 17 mins and 1 hour 48 mins in CPU time for $f_{>24}$ and f_D, respectively. For the production of the quiet variation $f_{FB,noSW}$, only the neural network for f_D is needed to be trained; this takes about 1 hour 48 mins in CPU time. When producing results on the test sets, it takes 6 seconds to produce 1 year of data. In summary, it takes about 5 hours in total in CPU time to train the neural networks for the results shown here.

6 Summary and Perspectives

We developed a novel approach based on machine-learning neural network to model the ground magnetic perturbations, characterized as the above-diurnal variation and the daily variation (Haberle et al., 2022), at CLF as driven by the solar and atmospheric variabilities. The sum of both variations, so called filter baseline produced from the filtering technique, f_{FB}, was reproduced using two neural networks with identical LSTM architecture. Using data from 1995 onwards, we trained each neural network along with the walk forward training that allows us to update the models with new data. Our modeled f_{FB} shows an overall good agreement with the original f_{FB} for both a solar-quiet year (2009) and a solar-active year (2012), with the Pcc values of 0.77 and 0.83, respectively, for the average of the x_{FB}, y_{FB}, and z_{FB} components. Importantly, by using only the F10.7 and geometrical parameters at CLF, we demonstrated that our neural networks can model the regular, quiet variation owing to the Sq variation. Our modeled quiet variation remains regular for both quiet and non-quiet periods, i.e. in the presence of geomagnetic storms, while capturing accurately the amplitude of the seasonal-dependent Sq variation. This latter aspect is a desirable quality for a geomagnetic baseline that would robustly discerns perturbed periods and provides a more-reliable magnetic activity index that reflects the actual intensity of geomagnetic storm perturbations.

Our work focused on data from CLF that is located at mid-latitude. The developed approach can be adapted to other magnetic observatories, although there can be local effects specific to geographical latitude and longitude. Our results at CLF show a less satisfactory result for x_{FB} (with average R^2 score of 0.1 - 0.5, compared to 0.6 - 0.8 of y_{FB} and z_{FB}), which can be influenced by the auroral and equatorial electrojets and ring current during the perturbed periods. Additionally, our model performance varies with the season with a better result in summer. More exploitable data related to the other contributing sources to the ground magnetic measurements, e.g., the neutral atmosphere, may improve our model. This work is a proof of concept that the neural networks can be used to predict the contributions to the ground magnetic measurements owing to the solar variabilities as well as the regular modulation owing to the daily and seasonal variabilities. Our future work will include a further optimization of the neural network workflow to improve its performance, an investigation of the neural network interpretability, and a consideration for future real-time applications in producing a reliable geomagnetic baseline as well as for predicting influence of the solar wind and solar transients at the ground level. Finally, our approach can be adapted for real-time and future forecasting of a magnetic activity index with high temporal resolution and fine intensity scale.

7 Open Research

The CLF magnetic observatory data are available from Bureau Central de Magnétisme Terrestre data repository (`http://doi.org/10.17616/R31NJMXR`) (*Bureau Central De Magnétisme Terrestre - BCMT*, 1921) and at Intermagnet data repository (`http://doi.org/10.17616/R3XK82`). We acknowledge use of NASA/GSFC's Space Physics Data Facilities (`http://doi.org/10.17616/R3P301`): OMNIWeb (`http://doi.org/10.17616/R3TH0D`), CDAWeb (`http://doi.org/10.17616/R39H0R`) and OMNI data.

Acknowledgments

The authors acknowledge the support of the French ANR (Agence Nationale de la Recherche), under grant ANR-20-ASTC-0030 (project ASTRID PRISMS). Work at IRAP is supported by Centre National de la Recherche Scientifique (CNRS), Centre National d'Etudes Spatiales (CNES), and the University of Toulouse III (UPS). Work at EOST is supported by CNRS, CNES, and the University of Strasbourg.

Appendix A Removing the secular trend

To remove the secular trend, we apply a rolling average on the sequential data using a specific window size centered at data point in consideration. The secular trend variation varies on the time scale between a month to a few thousand of years. On time scales of between a month and 100 years, the secular variation is entirely caused by the rigidly coupled movement of the magnetic field lines with the fluid motion in the liquid outer core (advection). In order to find an optimum window size for the trend removal, we preprocess the filter data by removing the rolling average with window sizes of 30, 45, and 90 days. For this experiment, we limit the training data for the neural network to 1997 - 2007 and use the validation data in 2008 as described in Section 3.2. Table A1 shows Pcc and R^2 values of individual components and the average values of all components (Pcc_{av} and R^2_{av}) of each model with a different window size for the trend removal. Considering the Pcc_{av}, the model using 45-day trend removal has the best value. However, it yields negative R^2_{av} as well as for the individual components. While the model using 90-day trend removal has a better Pcc_{av}, it has a lower R^2_{av} compared to the model using 30-day window. The model using 30-day window appears to be the best compromise.

Table A1. Pearson correlation coefficients (Pcc) and R^2 score of the "static" neural network model for the above diurnal components using various window sizes for the secular trend removal.

Window size (days)	Pcc [$x_{>24}$, $y_{>24}$, $z_{>24}$]	Pcc_{av}	R^2 [$x_{>24}$, $y_{>24}$, $z_{>24}$]	R^2_{av}
30	[0.658, 0.412, 0.535]	0.535	[0.341, 0.005, 0.105]	0.150
45	[0.734, 0.466, 0.578]	0.593	[-0.084, -0.103, -0.078]	-0.088
90	[0.722, 0.401, 0.557]	0.560	[0.201, -0.054, 0.215]	0.121

Appendix B Model performance for each month in 2009 and 2012

Table B1 shows the monthly performance of our modeled f_{FB} for 2009. Table B2 shows the monthly performance of our modeled f_{FB} for 2012. The model performance is assessed using Pcc and R^2 for the individual components, as well as the averages of the three component. The yearly average for Pcc and R^2 are also given.

Table B1. Pcc and R^2 score of the f_{FB} for each month in 2009.

Month	Pcc [x_{FB}, y_{FB}, z_{FB}]	Pcc_{av}	R^2 [x_{FB}, y_{FB}, z_{FB}]	R^2_{av}
Jan	[0.667, 0.714, 0.697]	0.693	[0.385, 0.362, 0.473]	0.407
Feb	[0.57, 0.747, 0.781]	0.699	[0.209, 0.43, 0.609]	0.416
Mar	[0.516, 0.82, 0.856]	0.731	[0.062, 0.626, 0.729]	0.472
Apr	[0.543, 0.93, 0.925]	0.799	[0.134, 0.85, 0.846]	0.61
May	[0.343, 0.923, 0.922]	0.729	[-0.178, 0.833, 0.85]	0.502
Jun	[0.825, 0.935, 0.848]	0.869	[0.624, 0.874, 0.674]	0.724
Jul	[0.768, 0.92, 0.829]	0.839	[0.566, 0.845, 0.674]	0.695
Aug	[0.705, 0.939, 0.816]	0.82	[0.467, 0.878, 0.637]	0.661
Sep	[0.677, 0.917, 0.84]	0.811	[0.252, 0.828, 0.695]	0.592
Oct	[0.718, 0.866, 0.845]	0.816	[0.226, 0.706, 0.694]	0.542
Nov	[0.701, 0.867, 0.801]	0.79	[0.076, 0.683, 0.624]	0.461
Dec	[0.399, 0.84, 0.591]	0.61	[-1.141, 0.424 , 0.267]	-0.15
Average	[0.619, 0.868, 0.813]	0.767	[0.140, 0.695, 0.648]	0.494

Table B2. Pcc and R^2 score of the f_{FB} for each month in 2012.

Month	Pcc [x_{FB}, y_{FB}, z_{FB}]	Pcc_{av}	R^2 [x_{FB}, y_{FB}, z_{FB}]	R^2_{av}
Jan	[0.797, 0.874, 0.7]	0.79	[0.546, 0.741, 0.42]	0.569
Feb	[0.698, 0.864, 0.792]	0.785	[0.423, 0.74, 0.595]	0.586
Mar	[0.798, 0.831, 0.874]	0.834	[0.607, 0.678, 0.751]	0.679
Apr	[0.684, 0.895, 0.89]	0.823	[0.439, 0.795, 0.776]	0.67
May	[0.714, 0.937, 0.915]	0.855	[0.509, 0.872, 0.838]	0.74
Jun	[0.809, 0.924, 0.877]	0.87	[0.63 , 0.85, 0.764]	0.748
Jul	[0.868, 0.905, 0.876]	0.883	[0.656, 0.793, 0.758]	0.736
Aug	[0.668, 0.953, 0.85]	0.824	[0.399, 0.907, 0.721]	0.676
Sep	[0.796, 0.931, 0.866]	0.864	[0.559, 0.864, 0.706]	0.71
Oct	[0.857, 0.921, 0.84]	0.873	[0.71, 0.844, 0.638]	0.731
Nov	[0.816, 0.868, 0.729]	0.804	[0.544, 0.718, 0.39]	0.551
Dec	[0.603, 0.861, 0.769]	0.744	[0.142, 0.703, 0.458]	0.434
Average	[0.759, 0.897, 0.832]	0.829	[0.514, 0.792, 0.651]	0.653

References

Abadi, M., Agarwal, A., Barham, P., Brevdo, E., Chen, Z., Citro, C., ... Zheng, X. (2015). *TensorFlow: Large-scale machine learning on heterogeneous systems.* Retrieved from `https://www.tensorflow.org/` (Software available from tensorflow.org)

Abuelezz, O. A., Mahrous, A. M., Cilliers, P. J., Fleury, R., Youssef, M., Nedal, M., & Yassen, A. M. (2021, February). Neural network prediction of the topside electron content over the Euro-African sector derived from Swarm-A measurements. *Advances in Space Research*, *67*(4), 1191-1209. doi: 10.1016/j.asr.2020.11.009

Alken, P., Maute, A., Richmond, A. D., Vanhamäki, H., & Egbert, G. D. (2017, May). An application of principal component analysis to the interpretation of ionospheric current systems. *Journal of Geophysical Research (Space Physics)*, *122*(5), 5687-5708. doi: 10.1002/2017JA024051

Bartels, J. (1949). The standardized index, ks, and the planetary index, kp. In H. H. Howe & E. K. Weisman (Eds.), *Iatme bulletin no. 12b, geomagnetic indices k and c, 1948* (p. 97). doi:10.25577/6zds-t813: IUGG.

Bartels, J., Heck, N. H., & Johnston, H. F. (1939, January). The three-hour-range index measuring geomagnetic activity. *Terrestrial Magnetism and Atmospheric Electricity*, *44*(4), 411. doi: 10.1029/TE044i004p00411

Bernoux, G., Brunet, A., Buchlin, É., Janvier, M., & Sicard, A. (2022, October). Forecasting the Geomagnetic Activity Several Days in Advance Using Neural Networks Driven by Solar EUV Imaging. *Journal of Geophysical Research (Space Physics)*, *127*(10), e2022JA030868. doi: 10.1029/2022JA030868

Brownlee, J. (2019). Introduction to time series forecasting with python. *Jason Brownlee*.

Bureau central de magnétisme terrestre - bcmt. (1921). French Global Network of Geomagnetic observatories [Data set]. Retrieved from `doi:10.18715/BCMT.MAG.DEF`

Campbell, W. H. (1989, September). An introduction to quiet daily geomagnetic fields. *Pure and Applied Geophysics*, *131*(3), 315-331. doi: 10.1007/BF00876831

Chakraborty, S., & Morley, S. K. (2020, July). Probabilistic prediction of geomagnetic storms and the K_p index. *Journal of Space Weather and Space Climate*,

10, 36. doi: 10.1051/swsc/2020037

Chapman, S. (1951, August). The equatorial electrojet as detected from the abnormal electric current distribution above Huancayo, Peru, and elsewhere. *Archives for Meteorology Geophysics and Bioclimatology Series A Meteorology and Atmopsheric Physics*, *4*(1), 368-390. doi: 10.1007/BF02246814

Collado-Villaverde, A., Muñoz, P., & Cid, C. (2021, June). Deep Neural Networks With Convolutional and LSTM Layers for SYM-H and ASY-H Forecasting. *Space Weather*, *19*(6), e02748. doi: 10.1029/2021SW002748

Collado-Villaverde, A., Muñoz, P., & Cid, C. (2023, August). Neural Networks for Operational SYM-H Forecasting Using Attention and SWICS Plasma Features. *Space Weather*, *21*(8), e2023SW003485. doi: 10.1029/2023SW003485

Efitorov, A. O., Myagkova, I. N., Shirokii, V. R., & Dolenko, S. A. (2018, November). The Prediction of the Dst-Index Based on Machine Learning Methods. *Cosmic Research*, *56*(6), 434-441. doi: 10.1134/S0010952518060035

Gjerloev, J. W. (2012). The supermag data processing technique. *Journal of Geophysical Research: Space Physics*, *117*(A9). doi: 10.1029/2012JA017683

Gruet, M. A., Chandorkar, M., Sicard, A., & Camporeale, E. (2018, November). Multiple-Hour-Ahead Forecast of the Dst Index Using a Combination of Long Short-Term Memory Neural Network and Gaussian Process. *Space Weather*, *16*(11), 1882-1896. doi: 10.1029/2018SW001898

Haberle, V., Marchaudon, A., Chambodut, A., & Blelly, P. L. (2022, August). Direct Determination of Geomagnetic Baselines During Quiet Periods for Low- and Mid-Latitude Observatories. *Journal of Geophysical Research (Space Physics)*, *127*(8), e30407. doi: 10.1029/2022JA030407

Hajra, R., & Sunny, J. V. (2022, March). Corotating Interaction Regions during Solar Cycle 24: A Study on Characteristics and Geoeffectiveness. *Solar Physics*, *297*(3), 30. doi: 10.1007/s11207-022-01962-1

Hochreiter, S., & Schmidhuber, J. (1997, 11). Long Short-Term Memory. *Neural Computation*, *9*(8), 1735-1780. doi: 10.1162/neco.1997.9.8.1735

Huang, S., Li, W., Shen, X.-C., Ma, Q., Chu, X., Ma, D., ... Goldstein, J. (2022, September). Application of Recurrent Neural Network to Modeling Earth's Global Electron Density. *Journal of Geophysical Research (Space Physics)*, *127*(9), e30695. doi: 10.1029/2022JA030695

Jackson, D. R., Bruinsma, S., Negrin, S., Stolle, C., Budd, C. J., Dominguez Gonzalez, R., ... Zhelavskaya, I. S. (2020, April). The Space Weather Atmosphere Models and Indices (SWAMI) project: Overview and first results. *Journal of Space Weather and Space Climate*, *10*, 18. doi: 10.1051/swsc/2020019

Jian, L., Russell, C. T., Luhmann, J. G., & Skoug, R. M. (2006). Properties of stream interactions at one au during 1995 –2004. *Solar Physics*, *239*(1), 337–392. doi: 10.1007/s11207-006-0132-3

Kaastra, I., & Boyd, M. (1996). Designing a neural network for forecasting financial and economic time series. *Neurocomputing*, *10*(3), 215-236. (Financial Applications, Part II) doi: 10.1016/0925-2312(95)00039-9

King, J. H., & Papitashvili, N. E. (2005, February). Solar wind spatial scales in and comparisons of hourly Wind and ACE plasma and magnetic field data. *Journal of Geophysical Research (Space Physics)*, *110*(A2), A02104. doi: 10.1029/2004JA010649

Kingma, D. P., & Ba, J. (2014). Adam: A method for stochastic optimization. *CoRR*, *abs/1412.6980*.

Kumluca, A., Tulunay, E., Topalli, I., & Tulunay, Y. (1999, November). Temporal and spatial forecasting of ionospheric critical frequency using neural networks. *Radio Science*, *34*(6), 1497-1506. doi: 10.1029/1999RS900070

Livermore, P. W., Finlay, C. C., & Bayliff, M. (2020, May). Recent north magnetic pole acceleration towards Siberia caused by flux lobe elongation. *Nature Geoscience*, *13*(5), 387-391. doi: 10.1038/s41561-020-0570-9

Lundberg, S. M., & Lee, S.-I. (2017). A unified approach to interpreting model predictions. In I. Guyon et al. (Eds.), *Advances in neural information processing systems* (Vol. 30). Curran Associates, Inc.

Lundstedt, H., Gleisner, H., & Wintoft, P. (2002, December). Operational forecasts of the geomagnetic Dst index. *Geophys. Res. Lett.*, *29*(24), 2181. doi: 10.1029/2002GL016151

Madsen, F. D., Beggan, C. D., & Whaler, K. A. (2022, October). Forecasting changes of the magnetic field in the United Kingdom from L1 Lagrange solar wind measurements. *Frontiers in Physics*, *10*, 1017781. doi: 10.3389/fphy.2022.1017781

Mayaud, P. N. (1967). *Atlas of indices k.* Paris: IUGG Publications.

Mayaud, P.-N. (1968). *Indices kn, ks et km, 1964-1967.* Faculté des sciences de Paris. Institut de physique du globe: Paris : Editions du Centre national de la recherche scientifique.

Menvielle, M., Iyemori, T., Marchaudon, A., & Nosé, M. (2011). Geomagnetic indices. In M. Mandea & M. Korte (Eds.), (Geomagnetic observations and models, IAGA Special Sopron Book Series ed., Vol. 5, p. 183-288). Dordrecht: Springer.

Menvielle, M., Papitashvili, N., Hakkinen, L., & Sucksdorff, C. (1995, December). Computer production of Kindices: review and comparison of methods. *Geophysical Journal International*, *123*(3), 866-886. doi: 10.1111/j.1365-246X.1995.tb06895.x

Myagkova, I. N., Shirokii, V. R., Kalegaev, V. V., Barinov, O. G., & Dolenko, S. A. (2021, January). The Use of Coupling Functions in the Forecasting of the Dst-Index Amplitude with Adaptive Methods. *Geomagnetism and Aeronomy*, *61*(1), 138-147. doi: 10.1134/S0016793220060092

Olsen, N., & Mandea, M. (2007, July). Will the Magnetic North Pole Move to Siberia? *EOS Transactions*, *88*(29), 293-293. doi: 10.1029/2007EO290001

Richardson, I. G., & Cane, H. V. (2010, June). Near-Earth Interplanetary Coronal Mass Ejections During Solar Cycle 23 (1996 - 2009): Catalog and Summary of Properties. *Solar Physics*, *264*(1), 189-237. doi: 10.1007/s11207-010-9568-6

Shin, D.-K., Lee, D.-Y., Kim, K.-C., Hwang, J., & Kim, J. (2016, April). Artificial neural network prediction model for geosynchronous electron fluxes: Dependence on satellite position and particle energy. *Space Weather*, *14*(4), 313-321. doi: 10.1002/2015SW001359

Siciliano, F., Consolini, G., Tozzi, R., Gentili, M., Giannattasio, F., & De Michelis, P. (2021, February). Forecasting SYM H Index: A Comparison Between Long Short Term Memory and Convolutional Neural Networks. *Space Weather*, *19*(2), e2020SW002589. doi: 10.1029/2020SW002589

Srivastava, N., Hinton, G., Krizhevsky, A., Sutskever, I., & Salakhutdinov, R. (2014, jan). Dropout: A simple way to prevent neural networks from overfitting. *J. Mach. Learn. Res.*, *15*(1), 1929–1958.

Stepanova, M. V., & Pérez, P. (2000, January). Autoprediction of Dst index using neural network techniques and relationship to the auroral geomagnetic indices. *Geofisica Internacional*, *39*(1), 143-146. doi: 10.22201/igeof.00167169p.2000.39.1.310

Sucksdorff, C., Pirjola, R., & Häkkinen, L. (1991). Computer production of k-indices based on linear elimination. *Geophys. Trans*, *36*, 333–345.

Tapping, K. F. (2013, July). The 10.7 cm solar radio flux ($F_{10.7}$). *Space Weather*, *11*(7), 394-406. doi: 10.1002/swe.20064

Tebabal, A., Radicella, S. M., Nigussie, M., Damtie, B., Nava, B., & Yizengaw, E. (2018, July). Local TEC modelling and forecasting using neural networks. *Journal of Atmospheric and Solar-Terrestrial Physics*, *172*, 143-151. doi: 10.1016/j.jastp.2018.03.004

Thébault, E., Purucker, M., Whaler, K. A., Langlais, B., & Sabaka, T. J. (2010, August). The Magnetic Field of the Earth's Lithosphere. *Space Sci Rev*, *155*(1-4), 95-127. doi: 10.1007/s11214-010-9667-6

Uwamahoro, J., & Habarulema, J. B. (2014, December). Empirical modeling of the storm time geomagnetic indices: a comparison between the local K and global Kp indices. *Earth, Planets and Space*, *66*, 95. doi: 10.1186/1880-5981-66-95

Vladimirov, R. D., Shirokiy, V. R., Myagkova, I. N., Barinov, O. G., & Dolenko, S. A. (2023, April). Comparison of the Efficiency of Machine Learning Methods in Studying the Importance of Input Features in the Problem of Forecasting the Dst Geomagnetic Index. *Geomagnetism and Aeronomy*, *63*(2), 161-171. doi: 10.1134/S0016793222600795

Wintoft, P., & Cander, L. R. (2000, March). Twenty-four hour predictions of f $_0$ F $_2$ using time delay neural networks. *Radio Science*, *35*(2), 395-408. doi: 10.1029/1998RS002149

Wu, J.-G., & Lundstedt, H. (1996, February). Prediction of geomagnetic storms from solar wind data using Elman Recurrent Neural Networks. *Geophys. Res. Lett.*, *23*(4), 319-322. doi: 10.1029/96GL00259

Yamazaki, Y., & Maute, A. (2017, March). Sq and EEJ—A Review on the Daily Variation of the Geomagnetic Field Caused by Ionospheric Dynamo Currents. *Space Sci Rev*, *206*(1-4), 299-405. doi: 10.1007/s11214-016-0282-z

Zhang, H., Xu, H. R., Peng, G. S., Qian, Y. D., Zhang, X. X., Yang, G. L., ... Zhu, M. B. (2022, October). A Prediction Model of Relativistic Electrons at Geostationary Orbit Using the EMD-LSTM Network and Geomagnetic Indices. *Space Weather*, *20*(10), e2022SW003126. doi: 10.1029/2022SW003126

Zhelavskaya, I. S., Shprits, Y. Y., & Spasojević, M. (2017, November). Empirical Modeling of the Plasmasphere Dynamics Using Neural Networks. *Journal of Geophysical Research (Space Physics)*, *122*(11), 11,227-11,244. doi: 10.1002/2017JA024406

Zou, Z., Shprits, Y. Y., Ni, B., Aseev, N. A., Zuo, P., & Wei, F. (2020, June). An artificial neural network model of electron fluxes in the Earth's central plasma sheet: a THEMIS survey. *Astrophysics and Space Science*, *365*(6), 100. doi: 10.1007/s10509-020-03819-0

Figure 1.

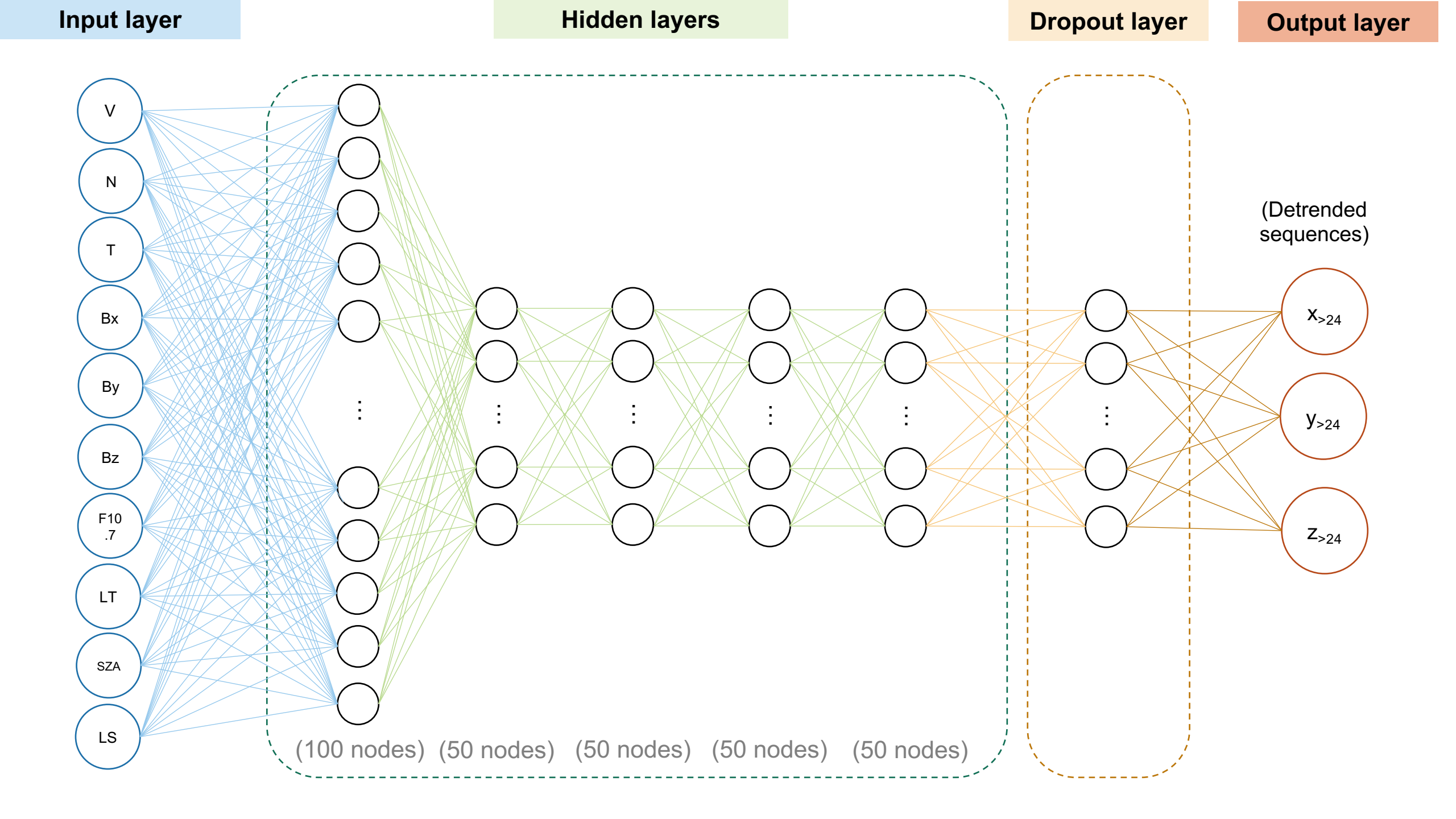
Input layer
Hidden layers
Dropout layer
Output layer
V
N
T
Bx
By
Bz
F10
.7
LT
SZA
LS
(100 nodes)
(50 nodes)
(50 nodes)
(50 nodes)
(50 nodes)
(Detrended
sequences)
x>24
y>24
z>24

Figure 2.

(a) **Above-diurnal filter workflow**

(a1) $f_{>24}$ → Trend removal

Solar wind & IMF (24-hr running average), F10.7, SZA, LT

(a2)

Scale the data

Structure the data for LSTM

Model with the neural network

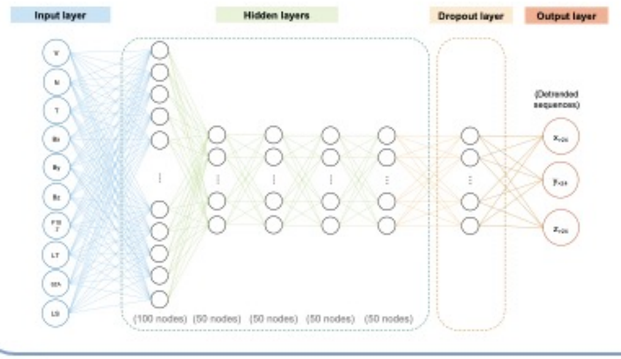

(a3) Rescale the data → Add the trend back → Modeled $f_{>24}$

(b) **Daily-filter workflow**

(b1) Compute $f_D = f_{24} + f_{12} + f_8 + f_6$ → f_D

Solar wind & IMF (24-hr running average), F10.7, SZA, LT

(b2)

Scale the data

Structure the data for LSTM

Model with the neural network

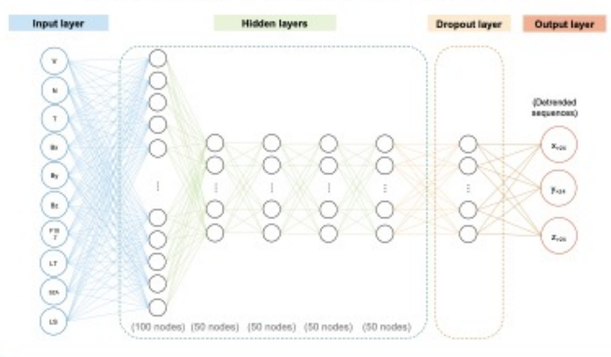

(b3) Rescale the data → Modeled f_D

(c) **Final product**

Compute modeled $\mathbf{f = f_{>24} + f_D}$

Figure 3.

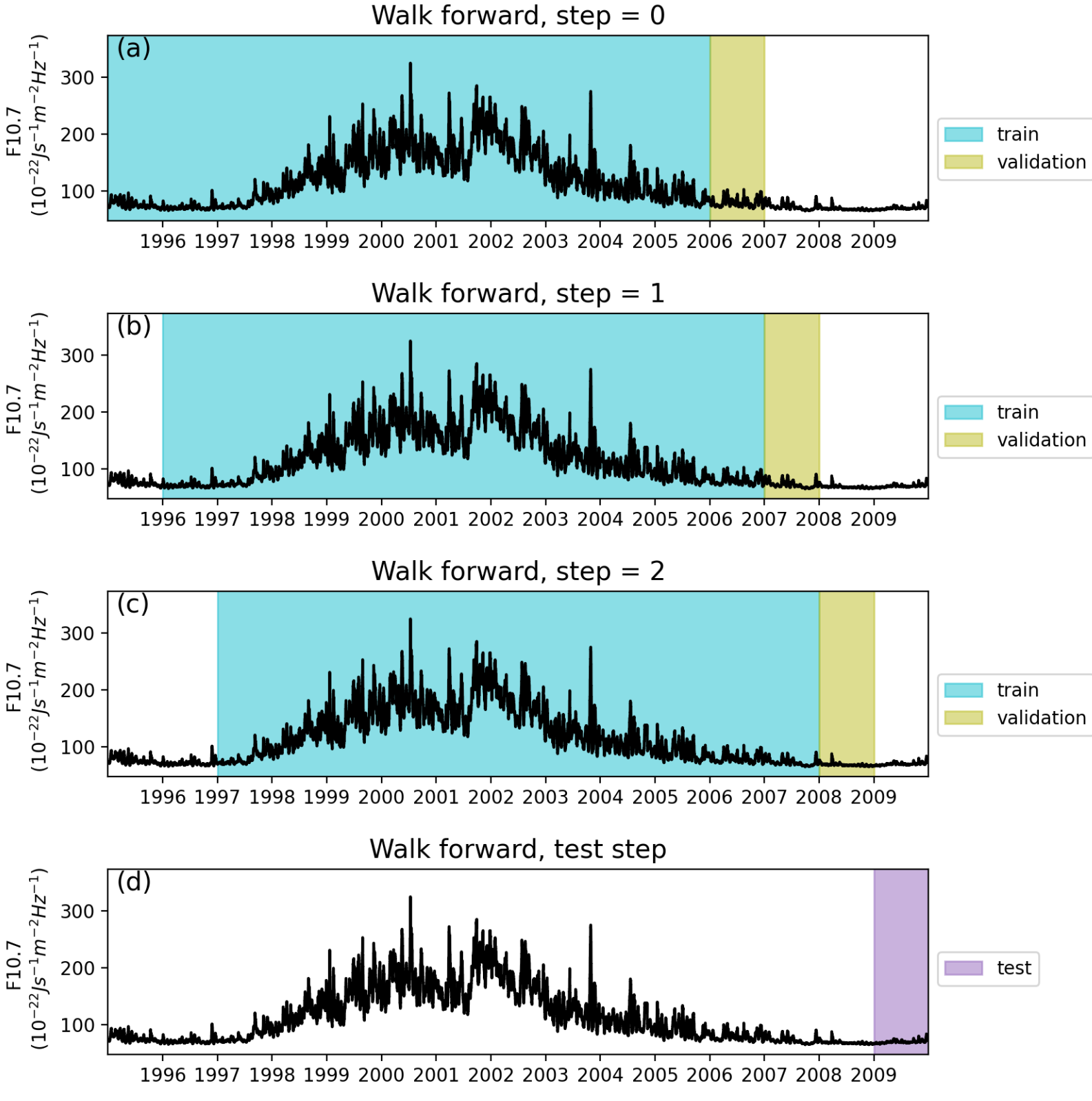
Walk forward, step = 0
(a)
F10.7
$(10^{-22}Js^{-1}m^{-2}Hz^{-1})$
300
200
100
1996 1997 1998 1999 2000 2001 2002 2003 2004 2005 2006 2007 2008 2009
train
validation
Walk forward, step = 1
(b)
F10.7
$(10^{-22}Js^{-1}m^{-2}Hz^{-1})$
300
200
100
1996 1997 1998 1999 2000 2001 2002 2003 2004 2005 2006 2007 2008 2009
train
validation
Walk forward, step = 2
(c)
F10.7
$(10^{-22}Js^{-1}m^{-2}Hz^{-1})$
300
200
100
1996 1997 1998 1999 2000 2001 2002 2003 2004 2005 2006 2007 2008 2009
train
validation
Walk forward, test step
(d)
F10.7
$(10^{-22}Js^{-1}m^{-2}Hz^{-1})$
300
200
100
1996 1997 1998 1999 2000 2001 2002 2003 2004 2005 2006 2007 2008 2009
test

Figure 4.

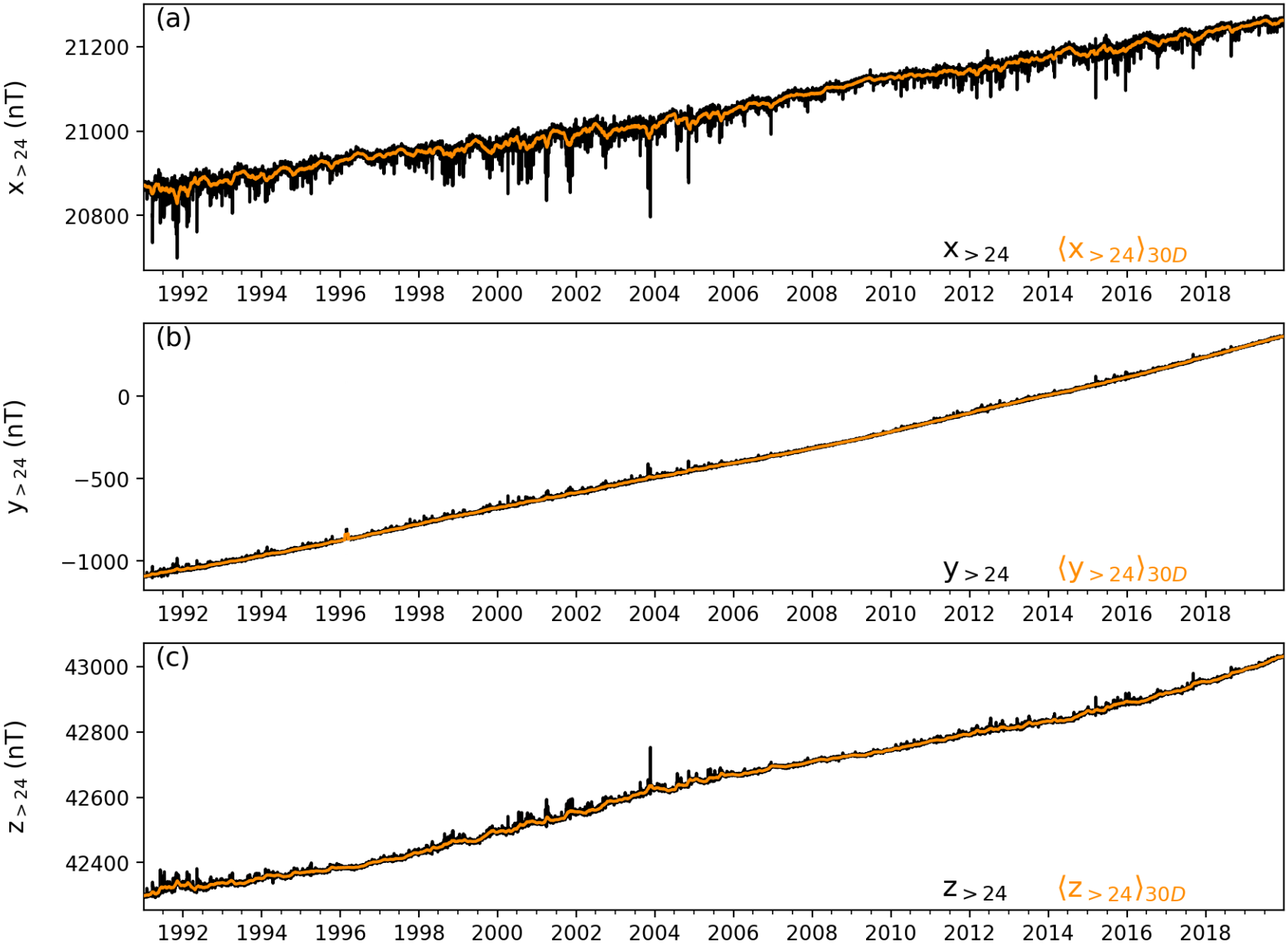
(a)
$x_{>24}$ (nT)
21200
21000
20800
$x_{>24}$
$\langle x_{>24} \rangle_{30D}$
(b)
$y_{>24}$ (nT)
0
−500
−1000
$y_{>24}$
$\langle y_{>24} \rangle_{30D}$
(c)
$z_{>24}$ (nT)
43000
42800
42600
42400
$z_{>24}$
$\langle z_{>24} \rangle_{30D}$
1992
1994
1996
1998
2000
2002
2004
2006
2008
2010
2012
2014
2016
2018

Figure 5.

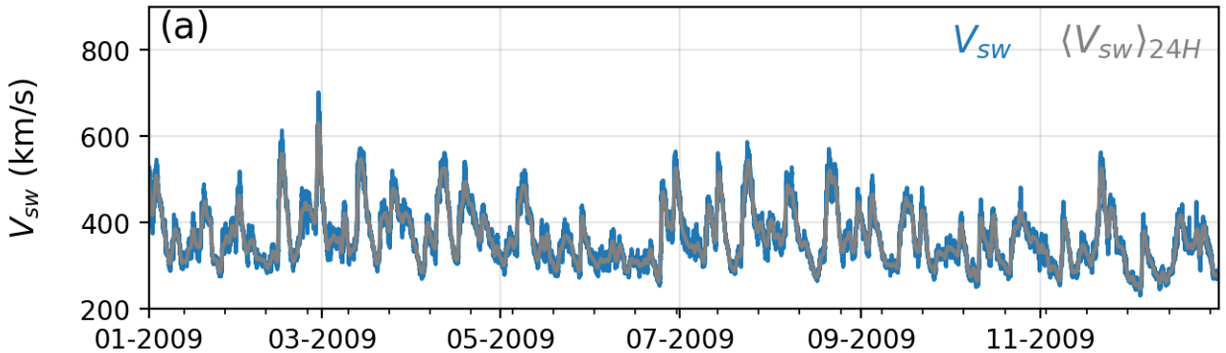
(a)
V_{sw}
$\langle V_{sw}\rangle_{24H}$
V_{sw} (km/s)
800
600
400
200
01-2009
03-2009
05-2009
07-2009
09-2009
11-2009

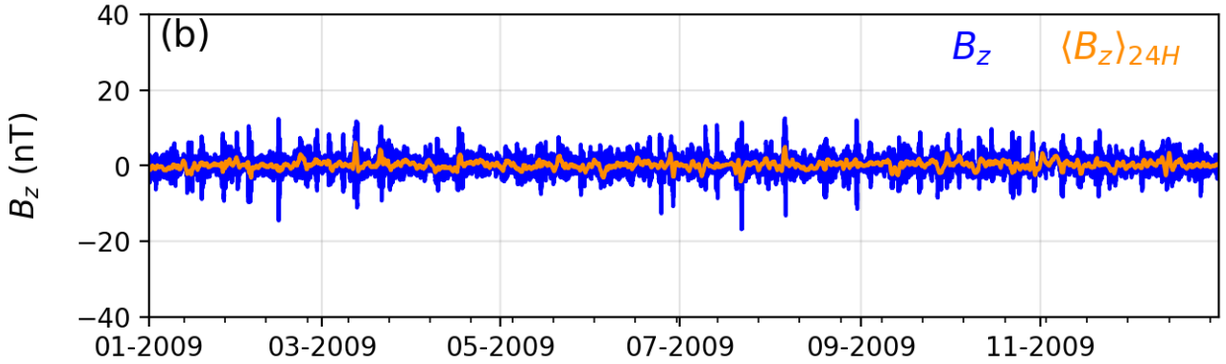
(b)
B_z
$\langle B_z\rangle_{24H}$
B_z (nT)
40
20
0
−20
−40
01-2009
03-2009
05-2009
07-2009
09-2009
11-2009

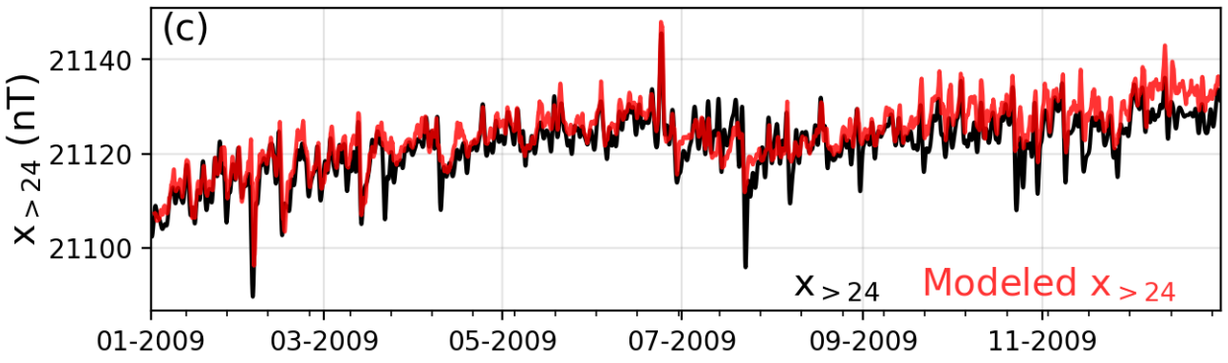
(c)
$x_{>24}$ (nT)
21140
21120
21100
$x_{>24}$
Modeled $x_{>24}$
01-2009
03-2009
05-2009
07-2009
09-2009
11-2009

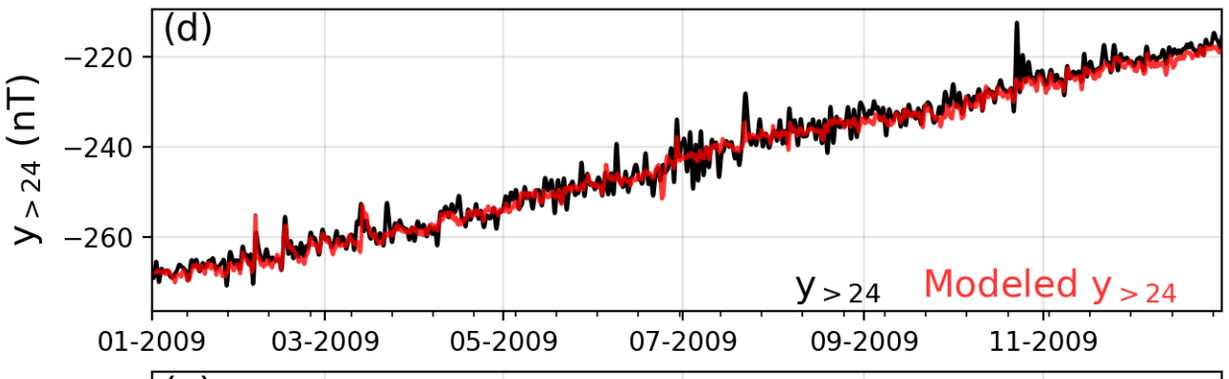
(d)
$y_{>24}$ (nT)
−220
−240
−260
$y_{>24}$
Modeled $y_{>24}$
01-2009
03-2009
05-2009
07-2009
09-2009
11-2009

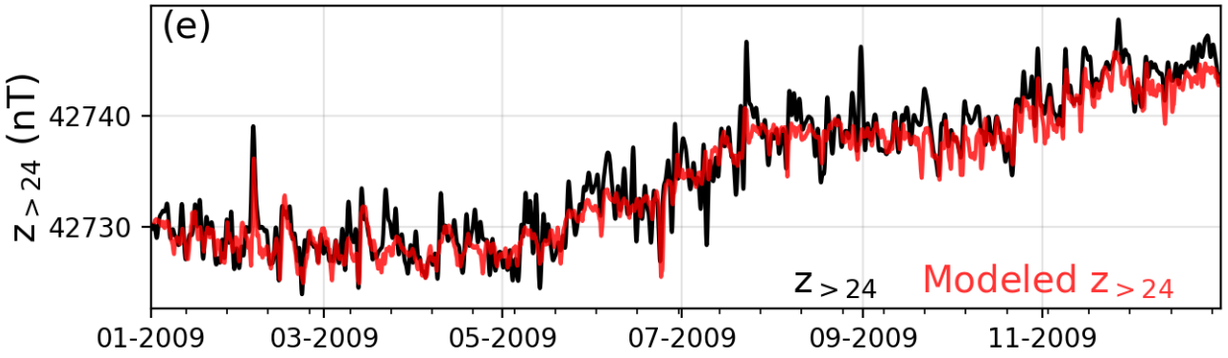
(e)
$z_{>24}$ (nT)
42740
42730
$z_{>24}$
Modeled $z_{>24}$
01-2009
03-2009
05-2009
07-2009
09-2009
11-2009

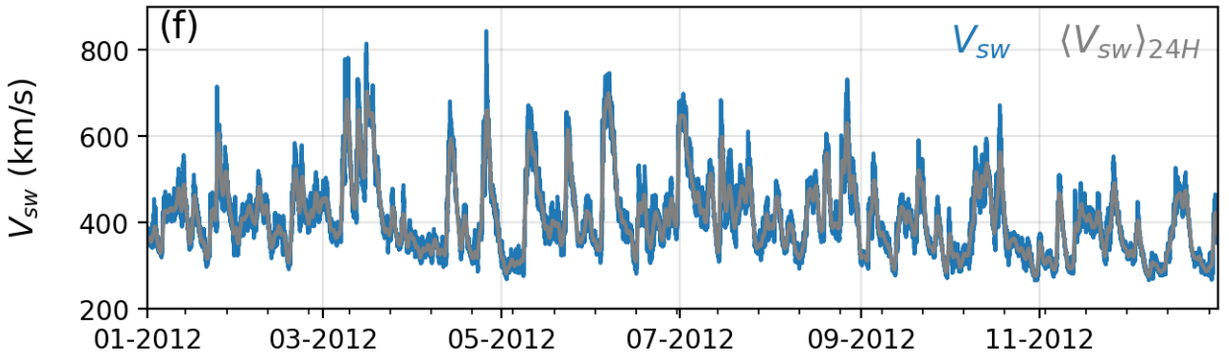
(f)
V_{sw}
$\langle V_{sw}\rangle_{24H}$
V_{sw} (km/s)
800
600
400
200
01-2012
03-2012
05-2012
07-2012
09-2012
11-2012

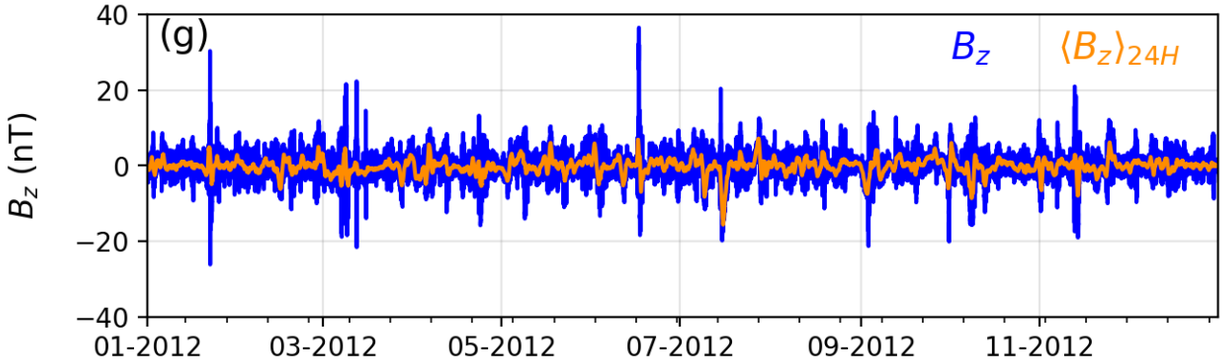
(g)
B_z
$\langle B_z\rangle_{24H}$
B_z (nT)
40
20
0
−20
−40
01-2012
03-2012
05-2012
07-2012
09-2012
11-2012

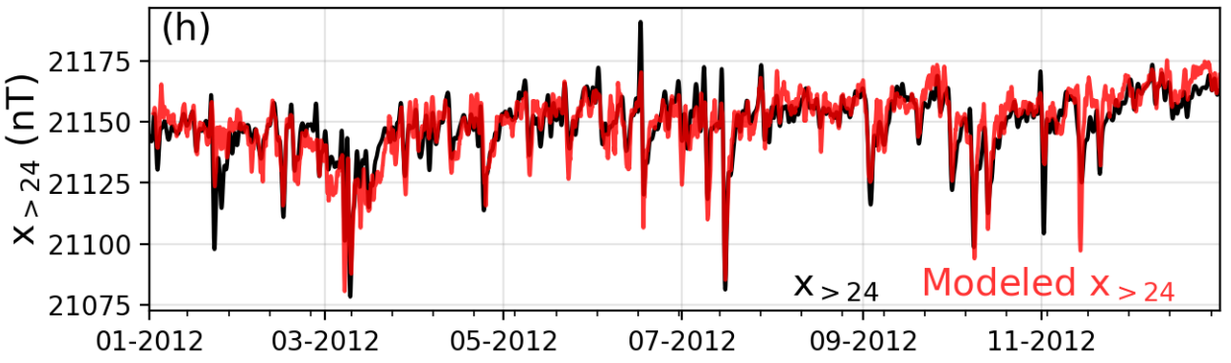
(h)
$x_{>24}$ (nT)
21175
21150
21125
21100
21075
$x_{>24}$
Modeled $x_{>24}$
01-2012
03-2012
05-2012
07-2012
09-2012
11-2012

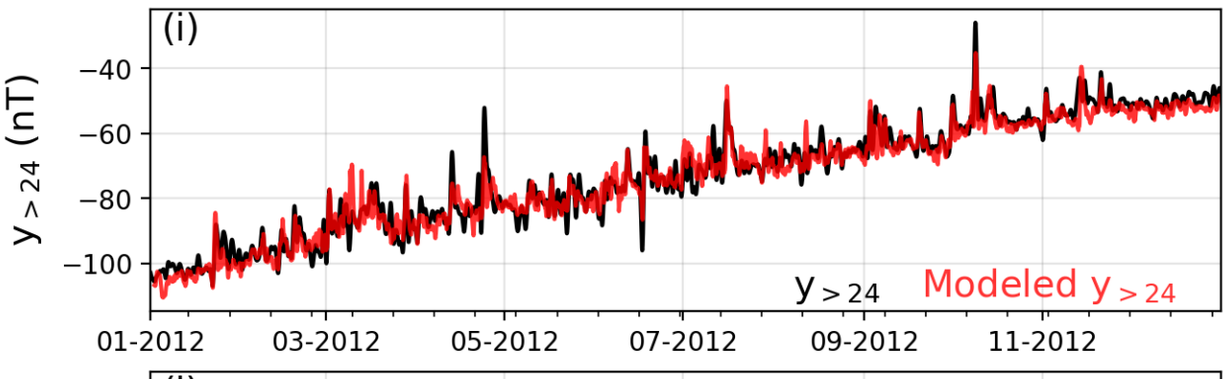
(i)
$y_{>24}$ (nT)
−40
−60
−80
−100
$y_{>24}$
Modeled $y_{>24}$
01-2012
03-2012
05-2012
07-2012
09-2012
11-2012

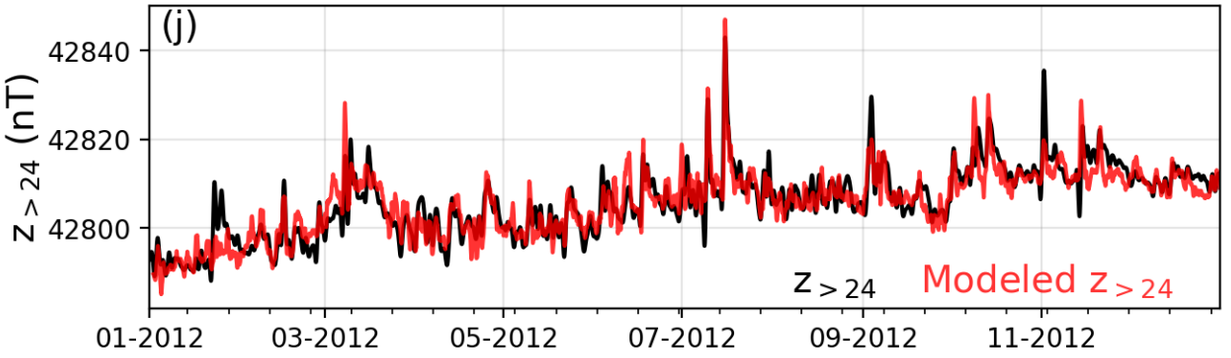
(j)
$z_{>24}$ (nT)
42840
42820
42800
$z_{>24}$
Modeled $z_{>24}$
01-2012
03-2012
05-2012
07-2012
09-2012
11-2012

Figure 6.

February 2009

(a)

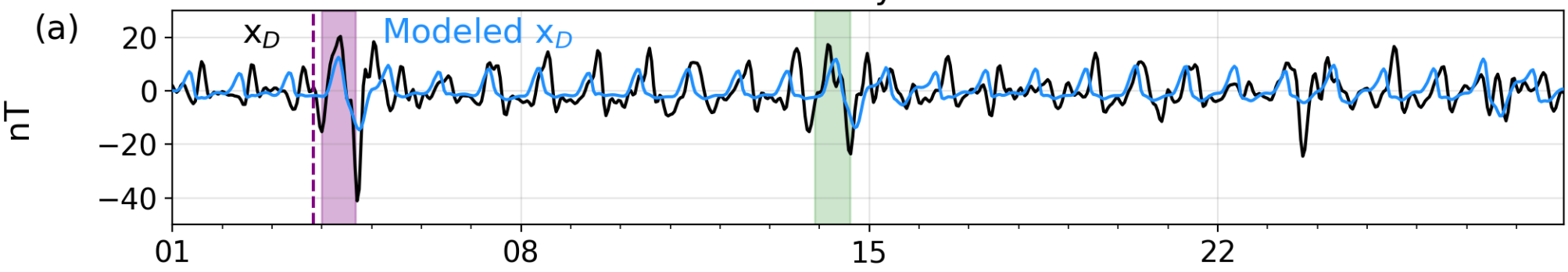

(b)

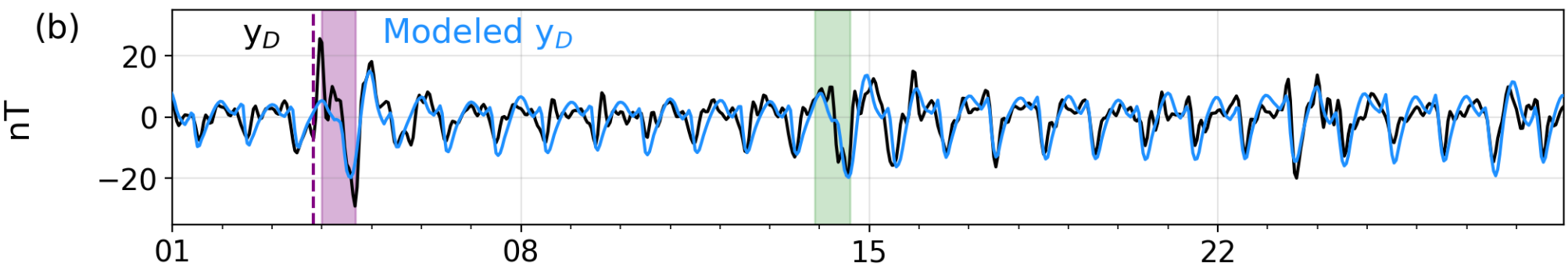

(c)

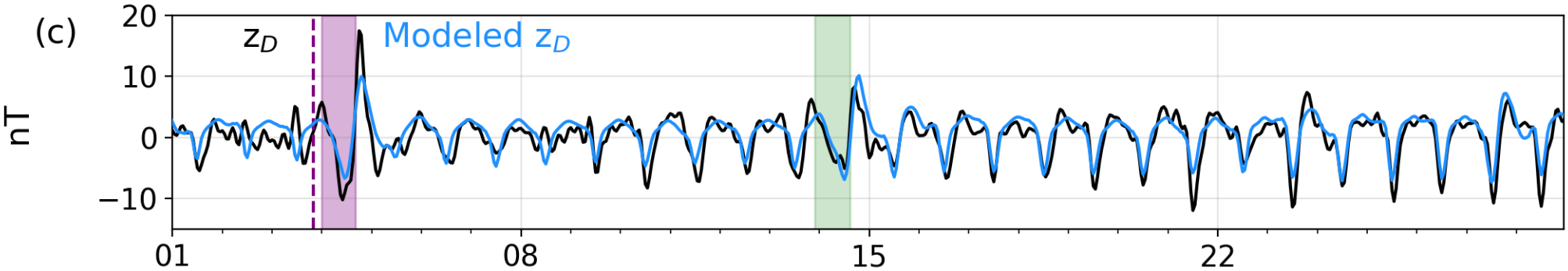

August 2009

(d)

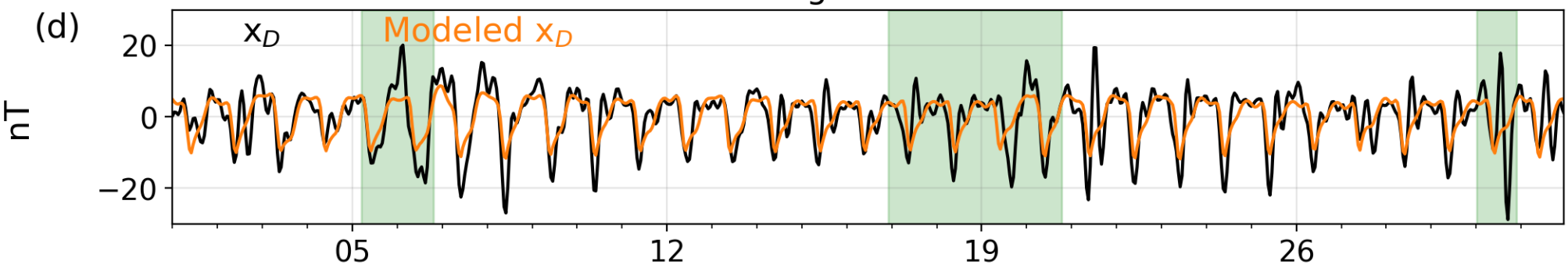

(e)

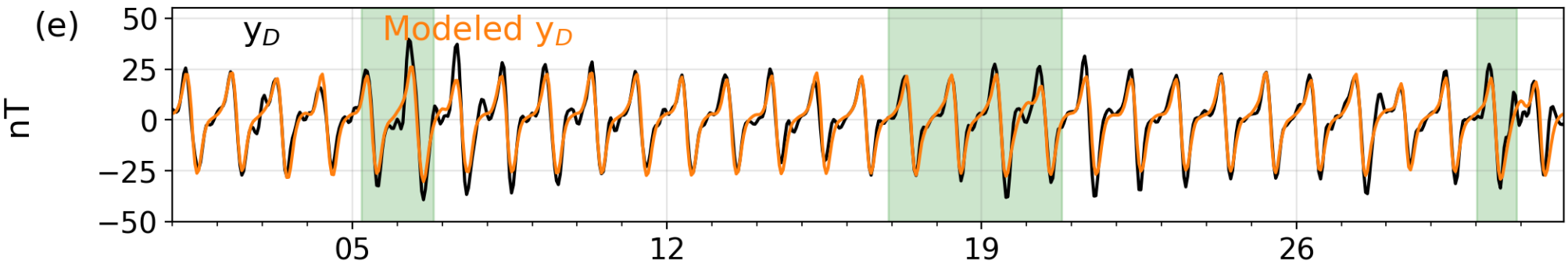

(f)

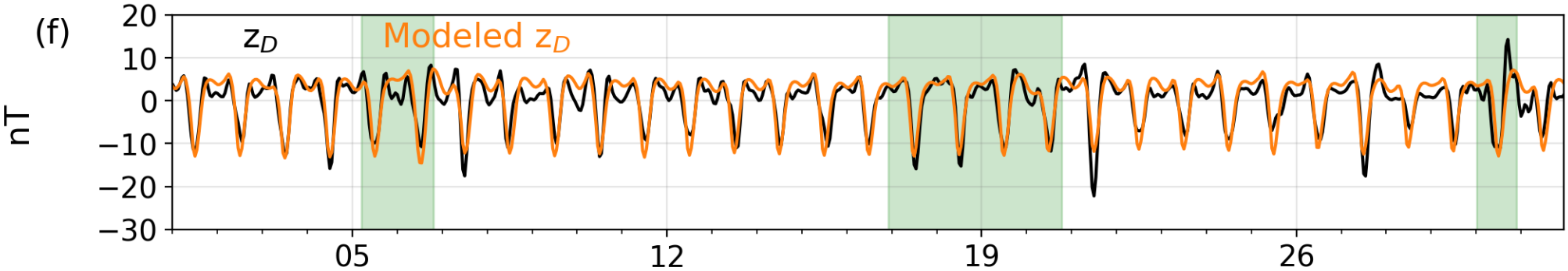

Figure 7.

January 2012

(a) x_D Modeled x_D

(b) y_D Modeled y_D

(c) z_D Modeled z_D

July 2012

(d) x_D Modeled x_D

(e) y_D Modeled y_D

(f) z_D Modeled z_D

nT

05 12 19 26

Figure 8.

February 2009

(a)

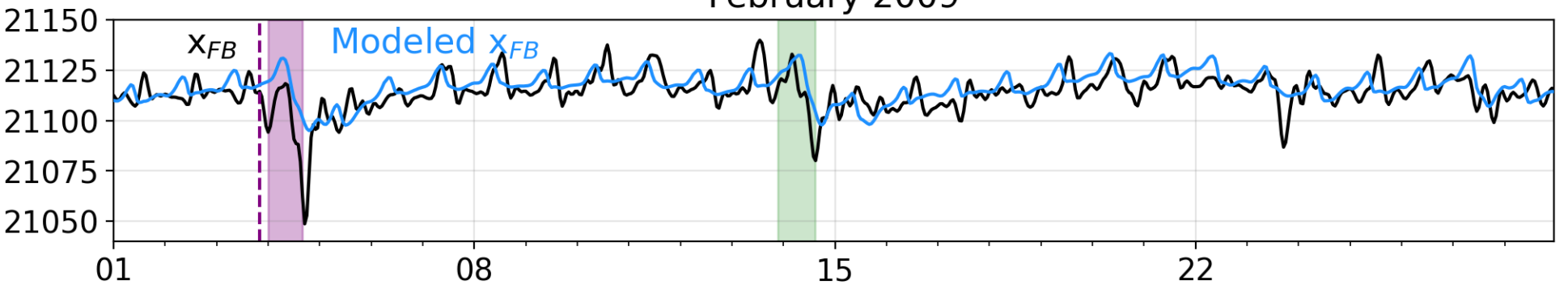

(b)

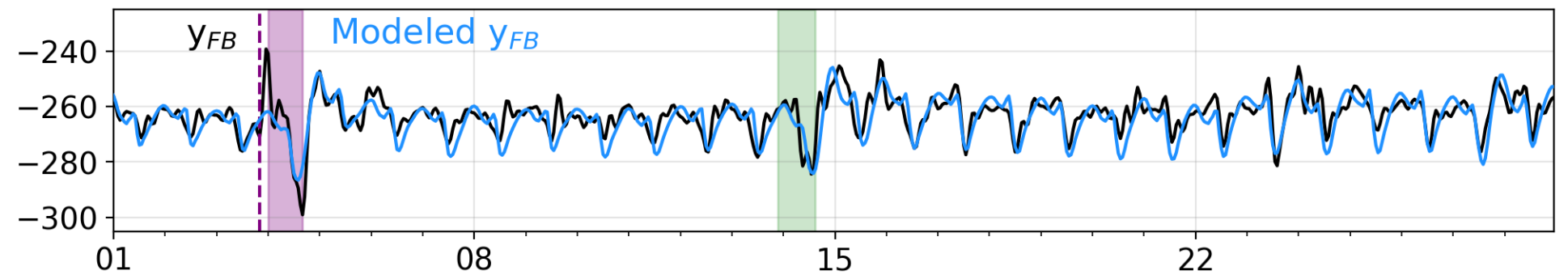

(c)

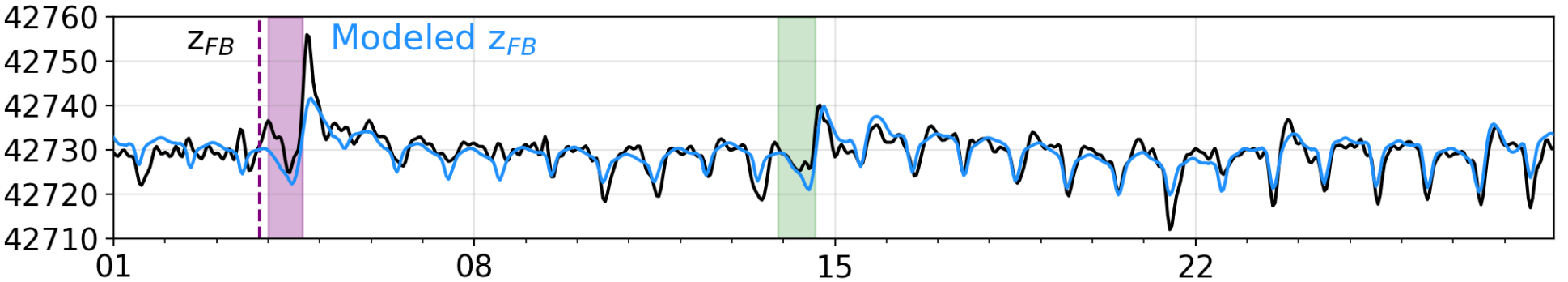

August 2009

(d)

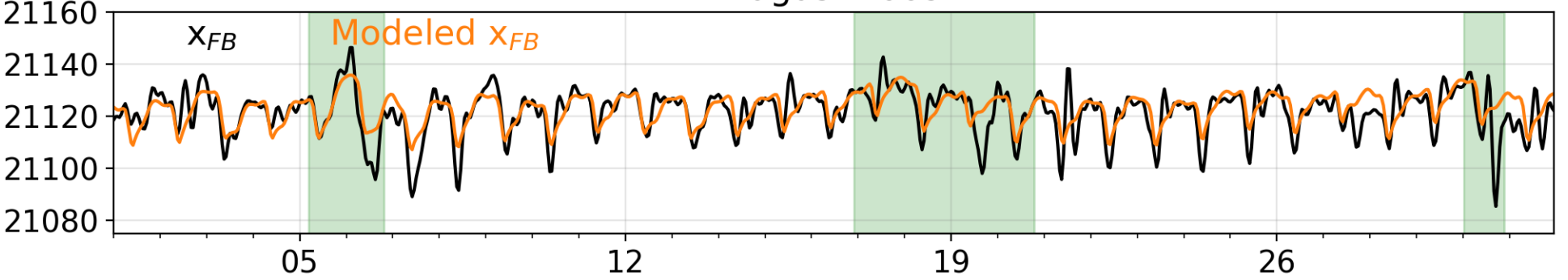

(e)

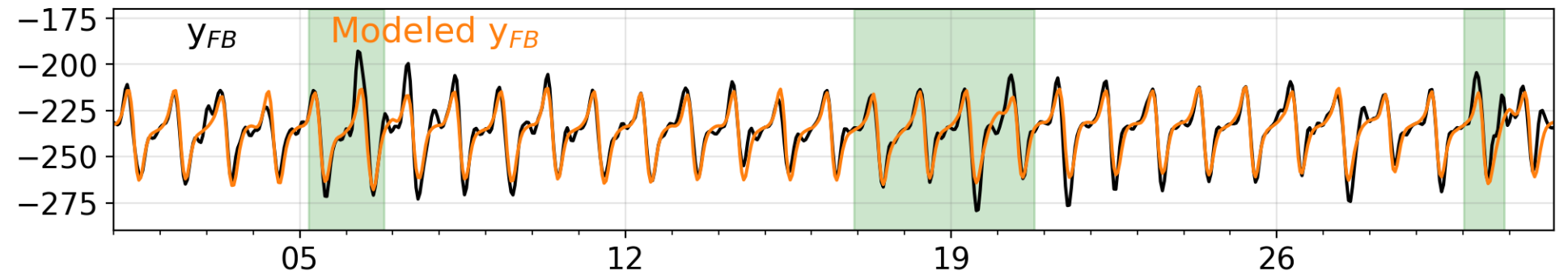

(f)

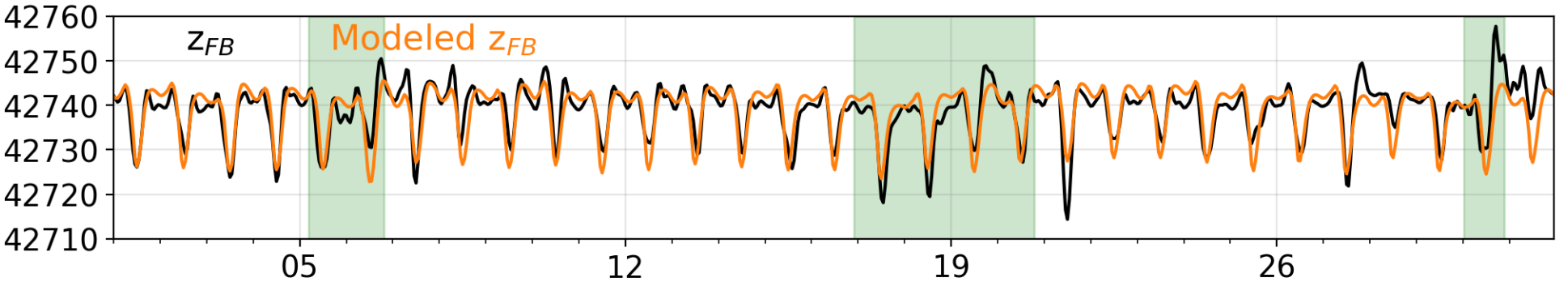

Figure 9.

January 2012

(a)

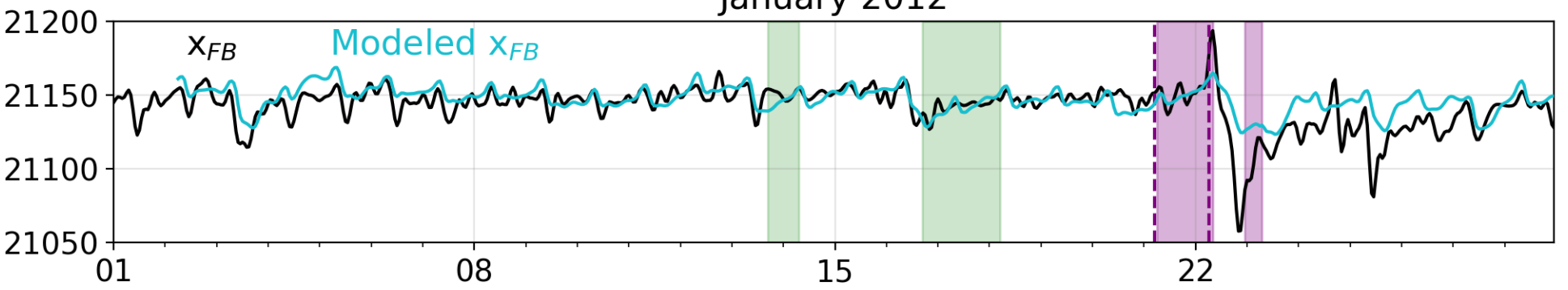

(b)

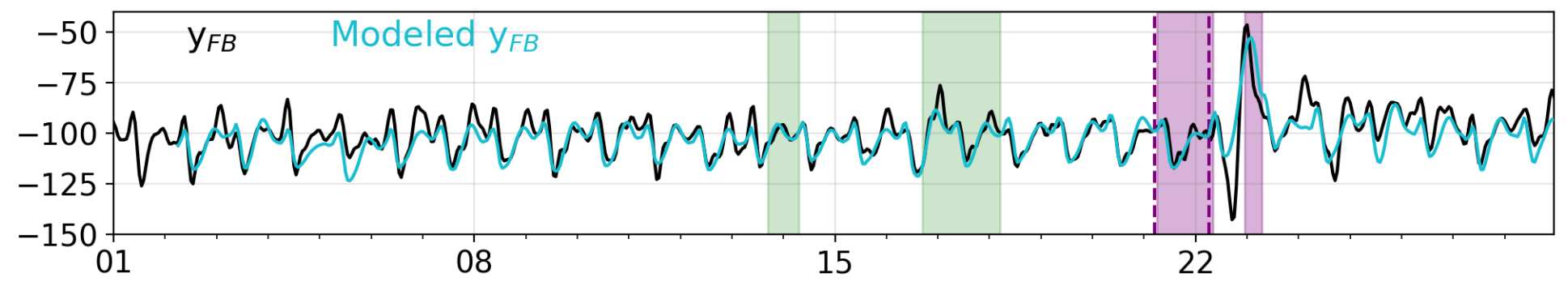

(c)

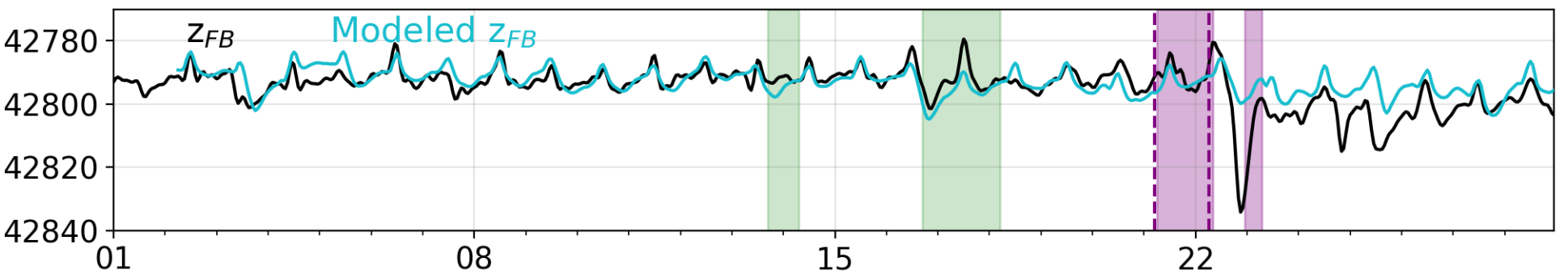

July 2012

(d)

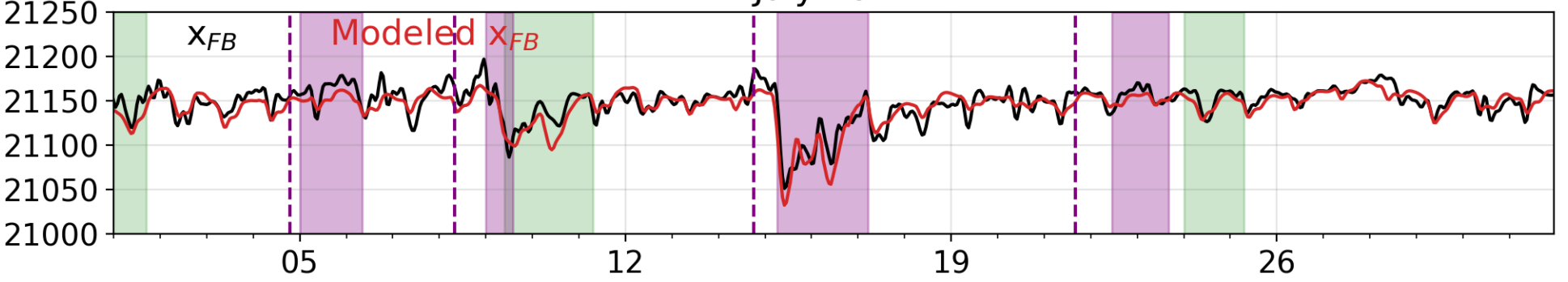

(e)

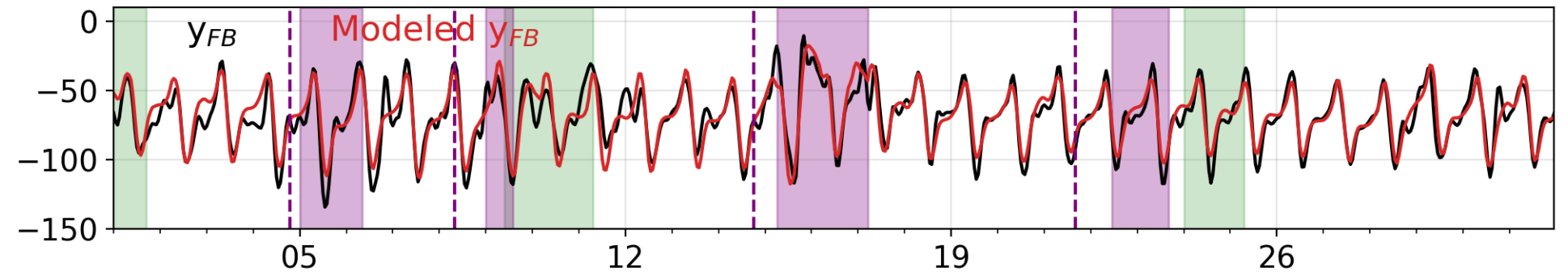

(f)

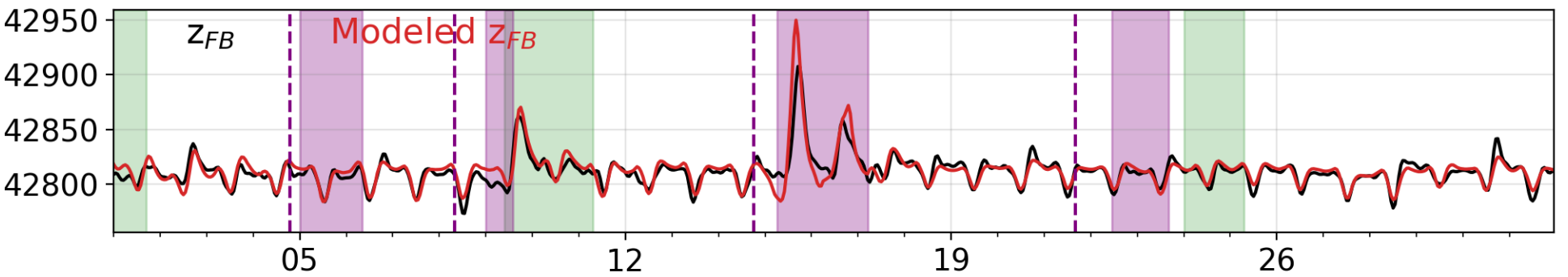

Figure 10.

August 2009

(a)

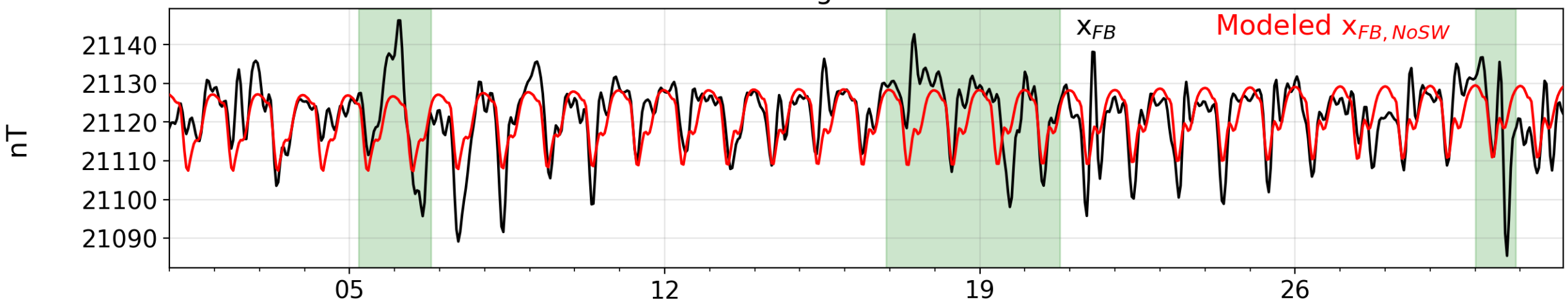

(b)

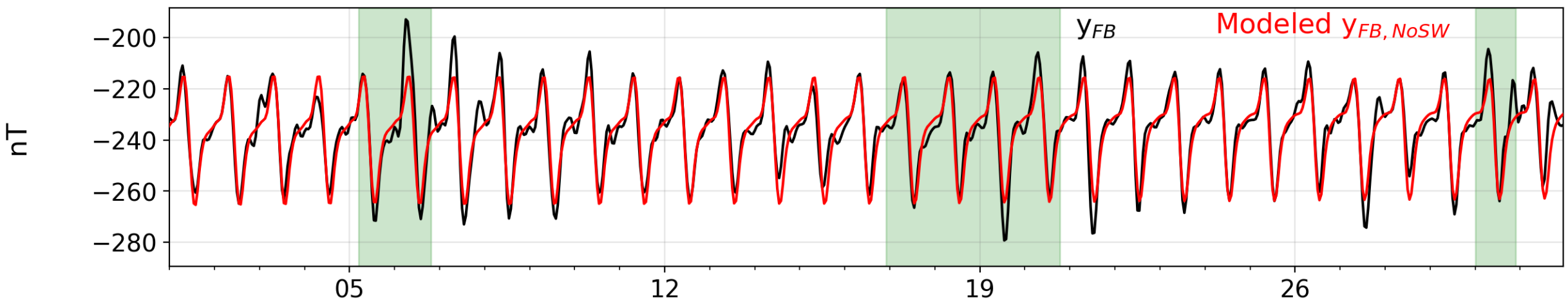

(c)

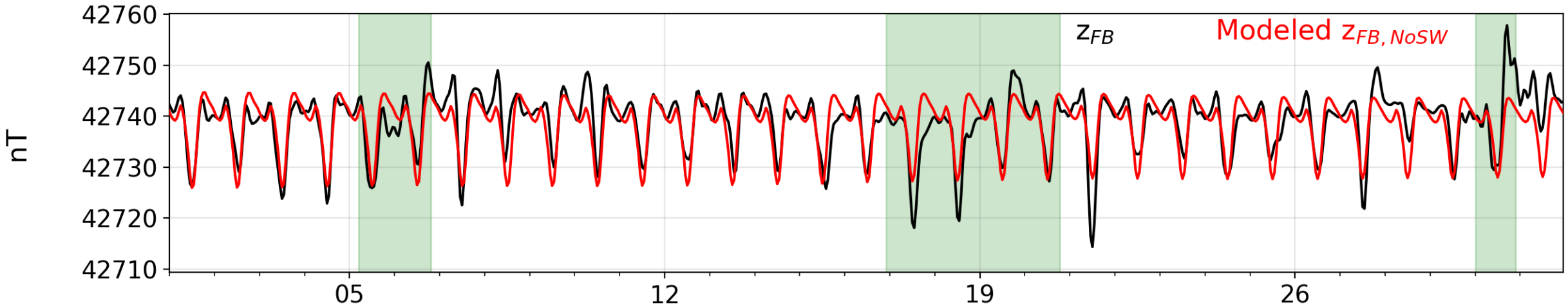

July 2012

(d)

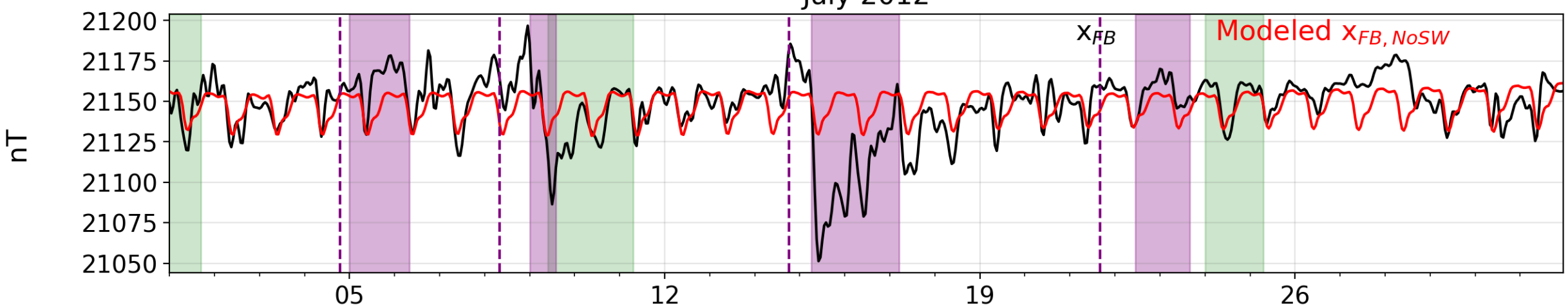

(e)

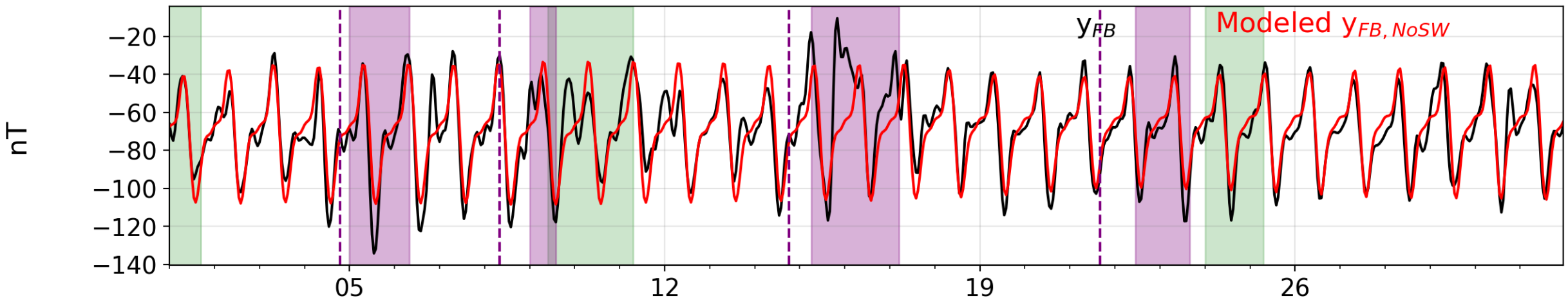

(f)